

# *The effect of horizontal resolution on the representation of the global monsoon annual cycle in Atmospheric General Circulation Models*

Article

Accepted Version

Zhang, L., Zhou, T., Klingaman, N. P., Wu, P. and Roberts, M. (2018) The effect of horizontal resolution on the representation of the global monsoon annual cycle in Atmospheric General Circulation Models. *Advances in Atmospheric Sciences*, 35 (8). pp. 1003-1020. ISSN 0256-1530 doi: <https://doi.org/10.1007/s00376-018-7273-9> Available at <http://centaur.reading.ac.uk/75426/>

It is advisable to refer to the publisher's version if you intend to cite from the work. See [Guidance on citing](#).

To link to this article DOI: <http://dx.doi.org/10.1007/s00376-018-7273-9>

Publisher: Science Press, co-published with Springer

All outputs in CentAUR are protected by Intellectual Property Rights law, including copyright law. Copyright and IPR is retained by the creators or other copyright holders. Terms and conditions for use of this material are defined in the [End User Agreement](#).

[www.reading.ac.uk/centaur](http://www.reading.ac.uk/centaur)

**CentAUR**

Central Archive at the University of Reading

Reading's research outputs online



**The effect of horizontal resolution on the representation of the global monsoon annual cycle in Atmospheric General Circulation Models**

Journal:	<i>Advances in Atmospheric Sciences</i>
Manuscript ID	AAS-2017-0273.R1
Manuscript Type:	Special Issue: CSSP (Submission deadline: 31 Oct. 2017)
Date Submitted by the Author:	n/a
Complete List of Authors:	Zhang, Lixia; IAP, LASG ZHOU, Tian-Jun; IAP, LASG Klingaman, Nicholas; University of Reading, National Centre for Atmospheric Science and Department of Meteorology Wu, Peili; Met Office, Hadley Centre Roberts, Malcolm J.; Met Office, Hadley Centre

SCHOLARONE™  
Manuscripts

1  
2  
3 1  
4  
5 2 **The effect of horizontal resolution on the representation of the global monsoon annu-**  
6  
7 **al cycle in Atmospheric General Circulation Models**  
8 3

9  
10  
11 4 Lixia Zhang<sup>1,2</sup>, Tianjun Zhou<sup>1</sup>, Nicholas P. Klingaman<sup>3</sup>, Peili Wu<sup>4</sup>, Malcolm Roberts<sup>4</sup>  
12  
13 5

14  
15 6 <sup>1</sup>*LASG, Institute of Atmospheric Physics, Chinese Academy of Sciences, Beijing, China*  
16  
17 7

18 <sup>2</sup>*Collaborative Innovation Center on Forecast and Evaluation of Meteorological Disasters,*  
19  
20 8 *Nanjing University of Information Science & Technology, Nanjing, China*  
21

22 9 <sup>3</sup>*National Centre for Atmospheric Science and Department of Meteorology, University of*  
23  
24 10 *Reading, Reading, United Kingdom*  
25

26  
27 11 <sup>4</sup> *Met Office Hadley Centre, Exeter, United Kingdom*  
28  
29

30 12 *Submitted to AAS CSSP special issue*  
31

32  
33  
34 13 *Revised on Jan, 2018*  
35

36  
37 14 **Corresponding author:**  
38

39 15 Dr. Lixia Zhang  
40

41  
42 16 LASG, Institute of Atmospheric Physics, Chinese Academy of Sciences,  
43

44 17 Beijing 100029, China.  
45

46  
47 18 Phone: 86-10-8299-5452  
48

49 19 Fax: 86-10-8299-5172  
50

51  
52 20 Email: [lixiazhang@mail.iap.ac.cn](mailto:lixiazhang@mail.iap.ac.cn)  
53  
54 21  
55 22  
56 23  
57 24  
58  
59  
60

1  
2  
3 25 **Abstract**  
4

5 26 The sensitivity of the representation of the global monsoon annual cycle to horizontal  
6  
7 27 resolution is compared in three Atmospheric General Circulation Models (AGCMs): the  
8  
9 28 Met Office Unified Model-Global Atmosphere 3.0 (MetUM-GA3), the Meteorological  
10  
11 29 Research Institute AGCM3 (MRI-AGCM3) and Global High Resolution AGCM from the  
12  
13 30 Geophysical Fluid Dynamics Laboratory (GFDL-HiRAM). For each model, we use two  
14  
15 31 horizontal resolution configurations for the period 1998–2008. Increasing resolution  
16  
17 32 consistently improves simulated precipitation and low-level circulation of the annual mean  
18  
19 33 and the first two annual cycle modes, as measured by pattern correlation coefficient and  
20  
21 34 Equitable Threat Score. Improvements in simulating the summer monsoon onset and  
22  
23 35 withdrawal are region-dependent. No consistent response to resolution is found in  
24  
25 36 simulating summer monsoon retreat. Regionally, increased resolution reduces the positive  
26  
27 37 bias in simulated annual mean precipitation, the two annual-cycle modes over the West  
28  
29 38 African monsoon and Northwestern Pacific monsoon. An overestimation of the solstitial  
30  
31 39 mode and an underestimation of the equinoctial asymmetric mode of the East Asian  
32  
33 40 monsoon are reduced in all high-resolution configurations. Systematic errors exist in  
34  
35 41 lower-resolution models for simulating the onset and withdrawal of the summer monsoon.  
36  
37 42 Higher resolution models consistently improve the early summer monsoon onset over East  
38  
39 43 Asia and West Africa, but substantial differences exist in the responses over Indian  
40  
41 44 monsoon region, where biases differ across the three low-resolution AGCMs. This study  
42  
43 45 demonstrates the importance of a multi-model comparison when examining the added  
44  
45 46 value of resolution and the importance of model physical parameterizations for the Indian  
46  
47 47 monsoon simulation.  
48

48 **Key Words** : global monsoon, high resolution modeling, annual cycle, AMIP  
49  
50  
51  
52  
53  
54  
55  
56  
57  
58  
59  
60

## 1. Introduction

Monsoons are characterized by a seasonal wet-dry contrast and a reversal of prevailing winds, due to the reversal of land-sea and inter-hemispheric thermal contrasts forced by the annual cycle of solar heating. The global monsoon is a dominant mode of annual variability of the global tropical circulation and is a response of the coupled climate system to annual variations in solar forcing (Wang and Ding 2008). Global monsoon regions sustain nearly two-thirds of the world's population and support some of the largest and fastest growing urban areas. The simulation and prediction of the annual cycle of monsoon circulation and precipitation is critically important, because of the effect of monsoons on hydrology, agriculture and local livelihoods and economies.

Although global monsoon regions are connected through mass conservation (Trenberth et al. 2000), each regional monsoon has unique characteristics due to the local interactions among the land surface, ocean, convection and synoptic weather systems, especially over Asian-Australian monsoon region. The well-recognized Asian summer monsoon system typically first onsets over the Bay of Bengal (BoB) in early May, followed by the South China Sea in mid-May and then India in early June (Wu and Zhang 1998; Xu and Chan 2001; Mao and Wu 2007). The onset over the BoB is often preceded by the development of a monsoon onset vortex (Krishnamurti and Ramanathan 1982; Wu et al. 2012). A numerical study by Liu et al. (2002) demonstrated that the onset of South China Sea monsoon is due to a Rossby wave train triggered by the strong latent heating during the BoB monsoon onset. The seasonal march of the East Asian summer monsoon (EASM) displays a step-wise northward and northeastward advance. From early May to mid-May, the ridge line of the western Pacific subtropical high (WPSH) is located along 15°N, and southern China experiences a pre-monsoon rainy season. Later, the WPSH exhibits two northward jumps in June and July with the ridge line located at 20°N and 25°N, respectively, the monsoon

1  
2  
3 74 rain band extends abruptly from the Indochina Peninsula – the South China Sea – from the  
4  
5 75 Philippines to the Yangtze River valley in early to mid-June, and the Meiyu (or Baiu in  
6  
7 76 Japan and Changma in Korea) begins. The monsoon penetrates into northern China (34-  
8  
9 77 41°N) in mid-July, and the monsoon rainy season there lasts for one month and ends in ear-  
10  
11 78 ly-middle August (Zhou et al. 2009). For the Australian summer monsoon onset in Decem-  
12  
13 79 ber, there are four major contributing factors, including land-sea thermal contrast, ba-  
14  
15 80 rotropic instability, arrival of the Madden-Julian oscillation (MJO) and intrusion of a mid-  
16  
17 81 latitude trough (Hung and Yanai 2004). The mean onset of the summer monsoon over  
18  
19 82 West Africa is 24th June, which is linked to an abrupt latitudinal shift of the Inter-Tropical  
20  
21 83 Convergence Zone (ITCZ) from a quasi-stationary location at 5°N in May-June to another  
22  
23 84 quasi-stationary location at 10°N in July-August (Sultan and Janicot 2003). For American  
24  
25 85 summer monsoon, the northward rainbelt movement over southwestern North America  
26  
27 86 from mid-to-late June is associated with the northward progression of the ITCZ (Yu and  
28  
29 87 Wallace 2000; Higgins and Shi 2001), while the onset of South American monsoon is re-  
30  
31 88 lated to eastward displacement of the South Atlantic subtropical high; it is also affected by  
32  
33 89 intraseasonal variability through low-frequency trough or ridge occurrence over southern  
34  
35 90 Brazil (Raia et al. 2008). The unique features of regional monsoons and their onset have  
36  
37 91 been rigorous metrics for gauging climate models' performances.  
38  
39  
40  
41  
42  
43  
44

45 92 The complexity of monsoon systems presents great challenges to simulate the climato-  
46  
47 93 logical seasonal means and annual cycles of the monsoon (Sperber et al. 2013; Zhou et al.  
48  
49 94 2017), although substantial efforts have been made to improve model physics and dynam-  
50  
51 95 ics in the past several decades. Model biases in the simulation of the monsoons limit the  
52  
53 96 fidelity of monsoon predictions and projections (Dong et al. 2016). Sperber et al. (2013)  
54  
55 97 evaluated the performance of 25 coupled climate models from Coupled Model Intercom-  
56  
57 98 parison Project Phase 5 (CMIP5) and 22 models from CMIP Phase 3 (CMIP3) in simulat-

1  
2  
3 99 ing the Asian summer monsoon onset and retreat. The authors found an overall delayed  
4  
5 100 onset over India in models, even though CMIP5 models showed improved fidelity relative  
6  
7 101 to CMIP3. The onset and retreat definition in Sperber et al. (2013) was based on rainfall  
8  
9 102 thresholds; monsoon onset might not occur in models, or may be delayed relative to obser-  
10  
11 103 vations, because of systematic dry biases. To avoid this issue, Sperber and Annamalai  
12  
13 104 (2014) proposed a fractional accumulation method to evaluate the monsoon annual cycle;  
14  
15 105 this method can be applied to many monsoon domains. The authors also found some sys-  
16  
17 106 tematic errors in the phase of rainfall annual cycle: coupled climate models in CMIP5 have  
18  
19 107 delayed onsets of summer rainfall over India, the Gulf of Guinea, and South America, but  
20  
21 108 early onsets for the Sahel and the North America.  
22  
23  
24  
25  
26

27 109 Several studies have proposed techniques to improve monsoon simulation, including in-  
28  
29 110 creasing horizontal resolution to capture more realistic large-scale atmospheric circulations  
30  
31 111 and precipitation distributions (Hack et al. 2006; Roberts et al. 2009; Demory et al. 2014 ;  
32  
33 112 Berckmans et al. 2013). The added value of resolution in GCMs has been widely verified  
34  
35 113 for many aspects of monsoon simulation (Kitoh et al., 2008; Mizuta et al., 2012; Johnson et  
36  
37 114 al., 2016). For example, an examination of version 5.1 of the National Center for Atmos-  
38  
39 115 pheric Research Community Atmosphere Model (CAM5) at three resolutions showed a  
40  
41 116 much better representation of the intensity-frequency structures of precipitation in steep-  
42  
43 117 terrain regions over East Asia (Li et al. 2015). Higher resolution in CAM5 also improves  
44  
45 118 the simulation of East Asian summer monsoon rain belt (Yao et al. 2017). Most investiga-  
46  
47 119 tions of the benefits of increased resolution were based on one model, however the sensi-  
48  
49 120 tivity to resolution may differ among models. Ogata et al. (2017) showed that the MRI-  
50  
51 121 AGCM3 and the MetUM-GA3 produced less precipitation over the western Pacific with  
52  
53 122 increasing resolution, but their sensitivity of Indian Ocean precipitation to resolution dif-  
54  
55 123 fered. Zhang et al. (2017) compared three AGCMs, each with two resolution configura-  
56  
57  
58  
59  
60



1  
2  
3 124 tions, and showed the sensitivity of monsoon precipitation to resolution varied greatly  
4  
5 125 among the models. To understand what aspects of resolution sensitivity are common  
6  
7 126 among AGCMs, it is important to compare several AGCMs using the same metrics. Given  
8  
9 127 the social and scientific importance of the onset and cessation of monsoon precipitation to  
10  
11 128 local livelihoods and economies, it is desirable to find whether high resolution systemati-  
12  
13 129 cally improves the representation of monsoon onset and withdrawal. This is the major mo-  
14  
15 130 tivation of the current study.  
16  
17  
18  
19

20 131 The remainder of the paper is organized as follows. The model simulations, validation  
21  
22 132 data and evaluation metrics are described in section 2. The improvement of high resolution  
23  
24 133 in simulating the annual cycle modes and summer monsoon onset and withdrawal are as-  
25  
26 134 sessed in section 3 and 4, respectively. Section 5 presents the summary and discussion.  
27  
28  
29

## 30 135 **2. Models, data and method description**

### 31 136 **2.1 Model simulations and observational validation datasets**

32  
33  
34 137 We use daily precipitation and monthly wind data from simulations with three AGCMs,  
35  
36 138 MetUM-GA3, MRI-AGCM3 and GFDL-HiRAM, each with two resolution configurations  
37  
38 139 for the period 1998–2008. Details of the models and experiments can be found in Table 1.  
39  
40 140 The model outputs of GFDL-HiRAM and MRI-AGCM3 were obtained from the Coupled  
41  
42 141 Model Intercomparison Project phase 5 data archive (Taylor et al., 2012). The simulations  
43  
44 142 of MetUM-GA3 are from the UPSCALE (UK on PRACE: weather-resolving Simulations  
45  
46 143 of Climate for global Environmental risk) project (Mizielinski et al., 2014). There are  
47  
48 144 very few different physical and dynamical settings in the MetUM-GA3 high-resolution  
49  
50 145 configuration compared to its low-resolution counterparts, mostly related to numerical  
51  
52 146 stability (Table 2 in Mizielinski et al. 2014). There are no physical parameter adjustments  
53  
54 147 between the MRI-AGCM3-2H and MRI-AGCM3-2S (Endo et al. 2012; Kusunoki 2016).  
55  
56 148 In GFDL-HiRAM, the shallow convective scheme and cloud microphysics are changed in  
57  
58  
59  
60

1  
2  
3 149 C360 from C180 (Zhao et al. 2009; Chen and Lin 2012). We analyze the ensemble mean of  
4  
5 150 all realizations of each model. Because of the large inter-model differences in dynamical  
6  
7  
8 151 cores and physics, it is hard to compare the resolution sensitivity across models. To ex-  
9  
10 152 clude the impact of model dependence and focus more on resolution, we compared the  
11  
12 153 high- and low-resolution configurations of the each model in this study.

14  
15 154 The observed daily precipitation datasets used in this study include (1) Tropical Rainfall  
16  
17 155 Measuring Mission (TRMM) 3B42 V7 (Huffman et al. 2007), to evaluate the climatologi-  
18  
19 156 cal mean state of global monsoon precipitation, at  $0.25^{\circ}\times 0.25^{\circ}$  resolution; and (2) Global  
20  
21 157 Precipitation Climatology Project V1.2 (GPCP), with a resolution  $1.0^{\circ}\times 1.0^{\circ}$  (Adler et al.  
22  
23 158 2003). In addition, monthly wind data from Climate Forecast System Reanalysis (CFSR;  
24  
25 159 Saha et al. 2010) with a resolution of  $0.5^{\circ}\times 0.5^{\circ}$  and from National Centers for Environmen-  
26  
27 160 tal Prediction–National Center for Atmospheric Research (NCEP–NCAR) reanalysis with  
28  
29 161 a resolution  $2.5^{\circ}\times 2.5^{\circ}$  (Kalnay et al. 1996) are used as the circulation datasets. All datasets  
30  
31 162 are interpolated to the N216 resolution of MetUM-GA3 (approximately  
32  
33 163  $0.83^{\circ}\text{longitude}\times 0.55^{\circ}\text{latitude}$ ) using a distance-weighted interpolation method, to facilitate  
34  
35 164 comparison. The longest common period of 1998–2008 covered by all simulations and ob-  
36  
37 165 servations is selected in the following analysis.

## 38 39 40 41 42 43 166 **2.2 Evaluation metrics on global monsoon annual cycles**

44  
45  
46 167 In this study, two aspects of the annual cycle of the global monsoon are evaluated: (1)  
47  
48 168 the mean climate and annual cycle modes and (2) monsoon onset and withdraw. As pro-  
49  
50 169 posed by Wang and Ding (2008), the annual mean, the solstitial (symmetric) and equinoc-  
51  
52 170 tial (asymmetric) modes of the annual cycle, and the global monsoon domain can be used  
53  
54 171 as metrics to gauge model performance for simulating the mean climate and annual cycle.  
55  
56 172 The solstitial mode is represented by the differences in precipitation or circulation between  
57  
58  
59  
60

1  
2  
3 173 June-September and December–March means; the equinoctial asymmetric mode is repre-  
4  
5 174 sented by the differences between April-May and October-November. The global monsoon  
6  
7  
8 175 domain is delineated both by the monsoon precipitation index (MPI) and zonal westerly  
9  
10 176 wind index (MWI). MPI is defined as the annual range of precipitation normalized by its  
11  
12 177 annual mean. MWI is similar, but using 850 hPa zonal wind (U850). The monsoon precipi-  
13  
14 178 tation domains are the areas where the annual range of precipitation exceeds 300mm and  
15  
16  
17 179 MPI exceeds 0.5, whereas monsoon wind domains are defined as WMI exceeding 0.5  
18  
19 180 without any restriction on the magnitude of annual range. The Annual range is the differ-  
20  
21 181 ence between May-September (MJJAS) and November-March (NDJFM) means in the  
22  
23 182 Northern Hemisphere, or NDJFM minus MJJAS in the Southern Hemisphere.

24  
25  
26 183 Previous studies have proposed several definitions of monsoon onset and withdrawal.  
27  
28 184 The commonly used definition is threshold-based (Wang and Lin 2002). One of the weak-  
29  
30 185 nesses of the threshold-based techniques is that monsoon onset might be delayed or accel-  
31  
32 186 erated by dry or wet biases, respectively, in the model, even though the model may have a  
33  
34 187 realistic annual cycle amplitude (Sperber et al. 2013; Sperber and Annamalai 2014). Mod-  
35  
36 188 els with dry biases are especially at a disadvantage since the observed threshold for defin-  
37  
38 189 ing monsoon may never be reached in such models, including MetUM-GA3 in this study  
39  
40  
41 190 (Bush et al. 2015; Johnson et al. 2016). Since the biases differ among the three models  
42  
43 191 used here, it is important to find a relatively fair way to evaluate onset and withdrawal in  
44  
45 192 models. Thus, a fractional accumulation approach is employed here. The monsoon onset  
46  
47 193 and withdrawal are defined as the pentad when the fractional accumulation first be-  
48  
49 194 comes  $\geq 0.2$  and  $\geq 0.8$ , respectively (Sperber and Annamalai 2014). The fractional accu-  
50  
51 195 mulated precipitation in a given pentad is the accumulated rainfall at that pentad divided by  
52  
53 196 the total accumulated rainfall at the end of the year. In this study, the pentads for the  
54  
55  
56  
57  
58  
59  
60

1  
2  
3 197 Southern African, Australian and South American domains have been reordered to run  
4  
5 198 from July 2 to June 27.  
6  
7

8 199 To quantitatively show the sensitivity of the simulated monsoon domain to resolution,  
9  
10 200 the Equitable Threat Score (ETS, Jolliffe and Stephenson 2003) is used in this study to  
11  
12 201 measure the simulation skill of the monsoon domain, which can be evaluated as a binary  
13  
14 202 event.  
15  
16

$$17 \quad \text{ETS} = (a - ar) / (a + b + c - ar) \quad (1)$$

18  
19 203 where  $ar = (a+b)(a+c)/n$ , represents the skill of a random prediction.  $a$ ,  $b$ , and  $c$  are the  
20  
21 204 counts of hits, false alarms and misses of monsoon domain, respectively, and  $n$  is the  
22  
23 205 number of model gridpoints in the region (45°S-45°N). The definition of each variable in  
24  
25 206 equation (1) can be found in Table 2. ETS ranges from 0 to 1 with perfect score of 1.  
26  
27  
28  
29

### 30 208 **3. Annual mean and annual cycle modes**

31  
32  
33 209 To investigate whether the improvement from higher-resolution is consistent across  
34  
35 210 the three models, we analyze the biases in the lower-resolution configuration and the dif-  
36  
37 211 ferences between the high- and low- resolution configurations. The bias in simulated an-  
38  
39 212 nual mean precipitation and improvements from higher resolution are presented in Fig.1. In  
40  
41 213 observations (blue lines in left panel of Fig.1), substantial precipitation falls in the Indo-  
42  
43 214 Pacific warm pool (60°E-180°), ITCZ and South Pacific Convergence Zone (SPCZ). In  
44  
45 215 general, the observed centers are well captured by the low-resolution configuration of each  
46  
47 216 AGCM, with an overall positive bias over most of the tropics (blue lines in right panel of  
48  
49 217 Fig.1). In contrast, there are several common biases among the three low-resolution  
50  
51 218 AGCMs, including overestimations over the southwest Indian Ocean, SPCZ, northern edge  
52  
53 219 of the ITCZ, and Northwestern Pacific Ocean, with underestimations over the southeastern  
54  
55 220 Indian Ocean (Fig.1 a, c, e). Unique biases in each AGCM are also found, particularly in  
56  
57  
58  
59  
60

1  
2  
3 221 MetUM-GA3 N216, which underestimates Indian and Maritime Continent precipitation  
4  
5 222 (Fig.1a). A positive bias over the western central Pacific ( $5^{\circ}\text{S}$ - $5^{\circ}\text{N}$ ,  $120^{\circ}\text{E}$ - $180^{\circ}$ ) is seen in  
6  
7 223 MRI-AGCM3-2H, while negative biases are present in MetUM-GA3 N216 and GFDL-  
8  
9 224 HiRAM-C180. A consistent response to higher resolution among the three models is sup-  
10  
11 225 pressed precipitation over the north of Maritime Continent (MC) and western Pacific ( $5^{\circ}\text{S}$ -  
12  
13 226  $15^{\circ}\text{N}$ ,  $120^{\circ}$ - $160^{\circ}\text{E}$ ), which partly reduces the wet bias over the Northwestern Pacific ( $5^{\circ}$ -  
14  
15 227  $15^{\circ}\text{N}$ ,  $120^{\circ}$ - $160^{\circ}\text{E}$ ) in the three low-resolution models. This consistent response to finer  
16  
17 228 resolution also has been illustrated by Ogata et al. (2017), which compared MetUM-GA3  
18  
19 229 and MRI-AGCM3. This is further verified with one additional model, GFDL-HiRAM. As  
20  
21 230 suggested by Ogata et al. (2017) and Johnson et al. (2016), the reduced precipitation over  
22  
23 231 the north of MC and western Pacific may be related to better-resolved steep topography  
24  
25 232 over MC and Indochina, with moisture convergence and precipitation on the windward  
26  
27 233 side of the orography, which leads to decreased moisture availability on the leeward side in  
28  
29 234 summer and reduced precipitation over the north of MC and western Pacific. This can be  
30  
31 235 partly seen from the difference between higher- and lower-resolution models in simulating  
32  
33 236 the solstitial mode in Fig.2. Note that the low-resolution of both MetUM-GA3 and GFDL-  
34  
35 237 HiRAM underestimate the precipitation over MC, and the consistent response to resolution  
36  
37 238 makes this dry bias even worse.

38  
39  
40  
41  
42  
43  
44  
45 239 As in Fig. 1, the biases in low-resolution models and improvement in higher- resolu-  
46  
47 240 tion configurations for the solstitial mode are shown in Fig. 2. The observed spatial pattern  
48  
49 241 shows an asymmetric contrast, with positive centers in Northern Hemisphere monsoon re-  
50  
51 242 gions (Indian-Pacific-East Asia, West Africa and northeast tropical Pacific ( $5^{\circ}$ - $20^{\circ}\text{N}$ ,  $120^{\circ}$ -  
52  
53 243  $60^{\circ}\text{W}$ )) and negative centers in Southern Hemispheric monsoon regions (South Africa,  
54  
55 244 Australia and South America; lines in left panel of Fig.2). The centers are well reproduced  
56  
57 245 by all low-resolution models, but all show underestimations over East Asia, the northeast  
58  
59  
60

1  
2  
3 246 tropical Pacific, South Africa and Australia region and overestimations over the northwest  
4  
5 247 Pacific (shading in left panel of Fig.2). Higher resolution reduces this consistent simulation  
6  
7  
8 248 bias, particularly over the northwest Pacific and northeast tropical Pacific (shading in left  
9  
10 249 panel of Fig.2). The improvement, however, is far smaller than the low-resolution model  
11  
12 250 bias. The biases in the three low-resolution models differ greatly over the Indian monsoon  
13  
14 251 region, where the solstitial mode is dramatically smaller than observation in MetUM-GA3  
15  
16 252 N216, greater in MRI-AGCM3-2H, and close to observation in GFDL-HiRAM-C180. The  
17  
18 253 sensitivity of the solstitial mode in each model to resolution also differs over the Indian  
19  
20 254 monsoon region. The inconsistency of model biases and sensitivity to resolution indicate  
21  
22 255 the strong role for sub-grid scale physical parameterizations for simulating the Indian mon-  
23  
24 256 soon precipitation.

257       The biases in the simulated equinoctial asymmetric mode of the annual cycle and cor-  
258 responding improvements in high-resolution models are shown in Fig. 3. In observations,  
259 negative values are centered in the zonal belt along (10°N-20°N), while positive values are  
260 centered to its south (0°-10°N) and in Southeast China. The centers over the Pacific repre-  
261 sent the asymmetric location of the spring and fall ITCZ (Wang and Ding 2008). The posi-  
262 tive values over Southeast China shows the region's characteristic spring-persistence sea-  
263 son in April and May (Li et al. 2017). All low-resolution models capture the asymmetric  
264 pattern of spring and fall precipitation, but a systematic overestimation over the Northern  
265 Hemisphere is seen in all models, with negative biases north of the observed negative cen-  
266 ter and positive biases near the observed positive centers. Positive biases over West Africa  
267 are found in all low-resolution models. In high-resolution models, the overestimation over  
268 Northwestern Pacific, West Africa and Southeast China is suppressed in all models; consis-  
269 tent improvements are also found over the southern Maritime Continent. This indicates  
270 increased resolution improves simulated precipitation in transition seasons.

1  
2  
3 271 To quantify the improvement in high-resolution models, the pattern correlation coef-  
4  
5 272 ficient (PCC) and root-mean-square-error (RMSE) of simulated precipitation over (45°S-  
6  
7 273 45°N) against TRMM are shown in Fig.4 a,d,g. The simulated 850 hPa winds for the an-  
8  
9 274 nual mean and the first annual cycle modes against CFSR reanalysis are also presented in  
10  
11 275 Fig.4. We compare the metrics for GPCP against TRMM and for NCEP-NCAR against  
12  
13 276 CFSR to show the observational uncertainty. In general, all low-resolution models simu-  
14  
15 277 late well the observed precipitation and 850 hPa wind patterns. For example, the PCCs  
16  
17 278 (RMSEs) of simulated annual mean precipitation and 850 hPa zonal (U850) and meridio-  
18  
19 279 nal wind (V850) in low resolution models (blue markers in Fig.4a-c) range from 0.85 to  
20  
21 280 0.90 (1.2 to 1.6 mm/day), 0.97 to 0.99 (0.75 to 1.2 m/s) and 0.88 to 0.94 (0.47 to 0.60 m/s),  
22  
23 281 respectively, which are close to those PCCs for GPCP and NCEP-NCAR against TRMM  
24  
25 282 and CFSR, respectively. The PCCs increase consistently in all three high-resolution models  
26  
27 283 (red markers) compared with their low-resolution counterparts (blue markers) for the three  
28  
29 284 annual-cycle metrics. However, the model bias as demonstrated by RMSE appears insensi-  
30  
31 285 tive to increasing resolution. The PCCs of annual precipitation, U850, V850 simulated by  
32  
33 286 high-resolution models are systematically shifted to right of the low-resolution ones, in-  
34  
35 287 creasing to 0.95~0.97, nearly 1.0 and 0.96~0.98, respectively. The PCCs in high-resolution  
36  
37 288 models are even higher than PCCs of GPCP/NCEP-NCAR, although the RMSEs in these  
38  
39 289 simulations are far larger than the reanalysis. The same results are also found in the first  
40  
41 290 two leading modes. High resolution aids in representing details of precipitation and circula-  
42  
43 291 tion distributions, but not in reducing model biases.

51  
52 292 Following the global monsoon domain definition proposed by Wang and Ding (2008),  
53  
54 293 the distributions of precipitation annual range and monsoon domain based on precipitation  
55  
56 294 are obtained and shown in Figure 5. In TRMM, the monsoon systems are well depicted by  
57  
58 295 this definition, including the Asian–Australian monsoon, the North and South African  
59  
60

1  
2  
3 296 monsoons, and the North and South American monsoons (Fig.5a). The domain obtained  
4  
5 297 from GPCP is similar to TRMM except at the edges, particularly over the northern edge of  
6  
7 298 the northwestern Pacific monsoon region and the southern edge of the southwestern Indian  
8  
9 299 Ocean monsoon region, where the domain areas are relatively larger in GPCP than in  
10  
11 300 TRMM. The North American monsoon region ( $120^{\circ}\text{W}$ - $60^{\circ}\text{W}$ ,  $0^{\circ}$ - $20^{\circ}\text{N}$ ) in all low-  
12  
13 301 resolution models is smaller and the western boundary is about 30 degrees eastward shifted  
14  
15 302 relative to observations, while the simulated northwestern Pacific monsoon is wider and  
16  
17 303 stronger than observations (left column in Fig.5). With increased resolution, the northwest-  
18  
19 304 ern Pacific monsoon region shrinks relative to the low-resolution models, particularly for  
20  
21 305 MRI-AGCM3, which extends to  $170^{\circ}\text{W}$  in MRI-AGCM3-2H but only to  $170^{\circ}\text{E}$  in MRI-  
22  
23 306 AGCM3-2S. Each model has unique biases, such as the absence of the Indian monsoon  
24  
25 307 region in MetUM-GA3 N216 due to its dry bias in India, a westward extended West Afri-  
26  
27 308 can monsoon ( $60^{\circ}\text{W}$ - $60^{\circ}\text{E}$ ,  $0^{\circ}$ - $20^{\circ}\text{N}$ ) in MetUM-GA3 N216 and MRI-AGCM3-2H due to a  
28  
29 309 wider and stronger ITCZ over the Atlantic Ocean, and an unrealistic monsoon region over  
30  
31 310 the southern tropical Atlantic Ocean in MRI-AGCM3-2H and GFDL-HiRAM-C180.  
32  
33 311 Those biases remain in their high-resolution counterparts, indicating little influence of res-  
34  
35 312 olution increase. Similar analysis of the global monsoon domain based on U850 revealed  
36  
37 313 no obvious improvements from increased resolution (Figure not shown).  
38  
39  
40  
41  
42  
43  
44

45 314 To quantitatively show the sensitivity of the simulated monsoon domain to resolution,  
46  
47 315 the Equitable Threat Score (ETS, Jolliffe and Stephenson 2003) for global and individual  
48  
49 316 regional monsoon domains was computed, using precipitation and U850 (Figure 6). Gener-  
50  
51 317 ally, higher-resolution configurations show slightly increased ETS for global monsoon pre-  
52  
53 318 cipitation (wind): from 0.53 to 0.54 (0.63 to 0.67) in MetUM-GA3, 0.56 to 0.57 (0.68 to  
54  
55 319 0.69) in GFDL-HiRAM and 0.58 to 0.62 (0.73 to 0.77) in MRI-AGCM3 models, respec-  
56  
57 320 tively. The ETS of the three high-resolution models for regional monsoon precipitation  
58  
59  
60



1  
2  
3 321 domains are not always higher than their low-resolution counterparts. Consistent improve-  
4  
5 322 ments with resolution are shown only for the South African monsoon domain, with the  
6  
7 323 largest increase from 0.59 to 0.64 in MetUM-GA3. The ETS for regional monsoon wind  
8  
9 324 domains are all higher in the high-resolution configurations. Note that the ETS metrics of  
10  
11 325 U850 and precipitation are not correlated. The skill scores of U850 are higher than those of  
12  
13 326 precipitation for both global and regional monsoons. Even though the higher-resolution  
14  
15 327 models show increased ETS for U850 for all regional monsoons except the East Asian  
16  
17 328 monsoon, the ETS metrics for precipitation do not increase (e.g., for the Indian monsoon).

#### 21 329 **4. Monsoon onset and withdrawal**

22  
23  
24 330 Cumulative rainfall, which is the sum of rainfall up to a given pentad, averaged over  
25  
26 331 each monsoon region is presented in Fig.7 to show the temporal characteristics of the rain-  
27  
28 332 fall and the model bias. A rapid increase in cumulative occurs in all monsoon regions.  
29  
30 333 However, the initial pentad for the rapid increase differs among regions, indicating dif-  
31  
32 334 ferent onset times in each region. For the Asian-Australian monsoon system, rapid precipi-  
33  
34 335 tation increase starts around pentad 30 in India, pentad 25 in Southeast Asia and East Asia,  
35  
36 336 and pentad 10 in Australia. Over the African and American monsoon systems, an onset is  
37  
38 337 observed in the pentad 30 in West Africa and North America, and pentad 5 in South Africa  
39  
40 338 and South America.

41  
42  
43  
44  
45 339 An overall overestimation of annual total precipitation is presented over all regional  
46  
47 340 monsoons except for India and Southeast Asia. For Indian monsoon, there is a large dispar-  
48  
49 341 ity among the models in simulated total rainfall. There is an obvious wet bias (50% wetter  
50  
51 342 than TRMM) in MRI-AGCM3, a dry bias (50% less than TRMM) in MetUM-GA3  
52  
53 343 AGCMs and a relatively small bias in GFDL-HiRAM (Fig. 7a). The biases over Southeast  
54  
55 344 Asia are similar to those over India, but with smaller magnitudes (Fig. 7b). The evolution  
56  
57 345 of precipitation accumulation shows that the bias is relatively small in the beginning of

1  
2  
3 346 year, but starts to increase around the monsoon onset pentad.  
4  
5

6 347 The observed and simulated spatial distributions of monsoon onset are shown in  
7  
8 348 Fig.8. The monsoon onset is the pentad when fractional accumulation first becomes  $\geq 0.2$   
9  
10 349 (Sperber and Annamalai 2014). We also examined the distributions of monsoon onset de-  
11  
12 350 fined by Wang and Lin (2002), in which onset is determined as the first pentad with the  
13  
14 351 relative rainfall rate to January mean in NH and July in SH exceeds  $5 \text{ mm d}^{-1}$ . This thresh-  
15  
16 352 old is never reached in MetUM-GA3 over India because of the systematic dry bias (Fig.1,  
17  
18 353 Fig. 2 and Fig.7a). However, India is defined as a monsoon region in MetUM-GA3 based  
19  
20 354 on the monsoon wind index (Figure not shown). Thus, it is reasonable to use the fractional  
21  
22 355 accumulation to define monsoon onset and withdrawal. To focus on monsoon regions, only  
23  
24 356 the distributions in the observed monsoon regions based on the monsoon precipitation in-  
25  
26 357 dex are shown here. In observations (Fig.8a-b), the onset pentad shows a gradual increase  
27  
28 358 from the equator to poleward, indicating later onset in the higher-latitude monsoon regions  
29  
30 359 in both hemispheres. In the NH, the earliest onset is pentad 25 in early May over the  
31  
32 360 southern edge of the Northern Hemispheric monsoon region and South China, while in the  
33  
34 361 SH the earliest onset is pentad 68 in early December over the northern edge of Southwest  
35  
36 362 Indian Ocean. The latest NH monsoon onset is at pentad 47 in mid-August over the north-  
37  
38 363 ern edge of the North American and West African monsoons (pentad 15 in mid-March  
39  
40 364 over the south edge of Australian monsoon in SH).  
41  
42  
43  
44  
45  
46  
47

48 365 All models simulate well the spatial distribution of global summer monsoon onset.  
49  
50 366 However, all low-resolution models simulate earlier monsoon onsets than the two observed  
51  
52 367 datasets, such as over the East Asian, West Africa monsoon, North American and South  
53  
54 368 American monsoon. Specifically, the area with onset by pentad 25 (hereafter P25 area)  
55  
56 369 over the West African, North American and East Asian monsoons is broader than in the  
57  
58 370 observation. In the high-resolution models, the P25 area slightly shrinks over the East  
59  
60

1  
2  
3 371 Asian and Western African monsoons, particularly apparent in MetUM-GA3. This differ-  
4  
5 372 ence is also seen in the observations, in which the P25 area in GPCP is larger than in  
6  
7  
8 373 TRMM, potentially due to the different resolutions of two observed datasets. It indicates  
9  
10 374 that high resolution improves the spatial distribution of precipitation and the delineation of  
11  
12 375 the monsoon onset boundaries. In other monsoon regions, there are no clear advantages of  
13  
14  
15 376 increased resolution.

16  
17  
18 377 As for the global monsoon onset, we compute distributions of monsoon withdrawal,  
19  
20 378 the pentad with fractional accumulation first becomes  $\geq 0.8$ , in simulations and observa-  
21  
22 379 tions (Fig. 9). The observed monsoon withdraws from higher latitudes toward the equatori-  
23  
24 380 al monsoon regions. In NH, the earliest withdrawal over East Asian monsoon is witnessed  
25  
26  
27 381 at pentad 48 in late August; the latest is over the southern edge of the Northern Hemi-  
28  
29 382 spheric monsoon region at pentad 60 in late October. In the SH, the earliest is over South  
30  
31 383 Africa at pentad 14 in mid-March and the latest over northern edge of Australia at pentad  
32  
33 384 30 in late June. The observed monsoon withdrawal patterns are well captured by all mod-  
34  
35  
36 385 els, but with relatively later withdrawals over the Australian and North American mon-  
37  
38 386 soons by two pentads. There are no obvious differences between the low- and high-  
39  
40 387 resolution configurations, or between GPCP and TRMM. These results suggest monsoon  
41  
42  
43 388 withdrawal is less sensitive to resolution than monsoon onset.

44  
45  
46 389 To quantitatively identify the improvements from higher resolution, the summer mon-  
47  
48 390 soon onset and withdrawal pentads averaged over each regional monsoon are shown in  
49  
50 391 Figure 10. In observations, TRMM shows (red dots in Fig. 10) that the monsoon onsets  
51  
52 392 (withdraws) at pentad 33 (52) over India, 30.5 (54) over Southeast Asia, 27.5 (49.5) over  
53  
54 393 East Asia, 7 (28.5) over Australia, 32.8 (53.5) over West Africa, 8.2 (27) over South Afri-  
55  
56 394 ca, 32.4 (56) over North America and 3.2 (27.2) over South America, respectively. Com-  
57  
58  
59 395 pared with TRMM, the onset pentads of all regional monsoons except the Indian monsoon

1  
2  
3 396 are systematically earlier in GPCP, the lower-resolution observational dataset, with the  
4  
5 397 largest difference of up to two pentads earlier in the West Africa monsoon. However, the  
6  
7 398 monsoon withdrawal dates from TRMM and GPCP are similar, with a maximum differ-  
8  
9  
10 399 ence of 0.5 pentad. The difference between TRMM and GPCP may suggest that resolution  
11  
12 400 has greater impact on monsoon onset than on withdrawal. For all domains the model dis-  
13  
14 401 persion far exceeds the differences between TRMM and GPCP. Here, we use the onset and  
15  
16 402 withdrawal derived from TRMM as a reference due to its higher resolution than GPCP.  
17  
18 403 All models show earlier onsets over East Asia, West Africa, South Africa and North Amer-  
19  
20 404 ica. The results are consistent with Fig.8 and Fig.9. Specifically, the largest bias is about  
21  
22 405 4.5 pentads in MRI-AGCM3-2H over East Asia, 4 pentads in GFDL-HiRAM-C180 over  
23  
24 406 West Africa, 2 pentads in GFDL-HiRAM-C360 over South Africa and 4.5 pentads in  
25  
26 407 GFDL-hIRAM-C360 over North America, respectively. Increased resolution consistently  
27  
28 408 delays the monsoon onset over East Asia and West Africa in all AGCMs, matching well  
29  
30 409 with the differences between TRMM and GPCP. However, these improvements from high  
31  
32 410 resolution are only one pentad at most, far less than the biases of the corresponding low-  
33  
34 411 resolution models ( $\leq 4.5$  pentad). A consistently slightly advanced onset in higher-  
35  
36 412 resolution models (1.5 pentad earlier at maximum over Southeast Asia) relative to their  
37  
38 413 lower-resolution counterparts is shown over Southeast Asia, Australia, South Africa, North  
39  
40 414 America and South America. For the Indian monsoon, both the biases of the lower-  
41  
42 415 resolution configurations and the improvement in the high-resolution configurations differ  
43  
44 416 greatly among the three AGCMs, indicating less resolution sensitivity of Indian monsoon  
45  
46 417 onset.

## 418 **5. Summary and discussion**

419 In this study, the resolution sensitivity of the annual cycle of the global monsoon is in-  
420  
421  
422  
423  
424  
425  
426  
427  
428  
429  
430  
431  
432  
433  
434  
435  
436  
437  
438  
439  
440  
441  
442  
443  
444  
445  
446  
447  
448  
449  
450  
451  
452  
453  
454  
455  
456  
457  
458  
459  
460  
461  
462  
463  
464  
465  
466  
467  
468  
469  
470  
471  
472  
473  
474  
475  
476  
477  
478  
479  
480  
481  
482  
483  
484  
485  
486  
487  
488  
489  
490  
491  
492  
493  
494  
495  
496  
497  
498  
499  
500  
501  
502  
503  
504  
505  
506  
507  
508  
509  
510  
511  
512  
513  
514  
515  
516  
517  
518  
519  
520  
521  
522  
523  
524  
525  
526  
527  
528  
529  
530  
531  
532  
533  
534  
535  
536  
537  
538  
539  
540  
541  
542  
543  
544  
545  
546  
547  
548  
549  
550  
551  
552  
553  
554  
555  
556  
557  
558  
559  
560  
561  
562  
563  
564  
565  
566  
567  
568  
569  
570  
571  
572  
573  
574  
575  
576  
577  
578  
579  
580  
581  
582  
583  
584  
585  
586  
587  
588  
589  
590  
591  
592  
593  
594  
595  
596  
597  
598  
599  
600  
601  
602  
603  
604  
605  
606  
607  
608  
609  
610  
611  
612  
613  
614  
615  
616  
617  
618  
619  
620  
621  
622  
623  
624  
625  
626  
627  
628  
629  
630  
631  
632  
633  
634  
635  
636  
637  
638  
639  
640  
641  
642  
643  
644  
645  
646  
647  
648  
649  
650  
651  
652  
653  
654  
655  
656  
657  
658  
659  
660  
661  
662  
663  
664  
665  
666  
667  
668  
669  
670  
671  
672  
673  
674  
675  
676  
677  
678  
679  
680  
681  
682  
683  
684  
685  
686  
687  
688  
689  
690  
691  
692  
693  
694  
695  
696  
697  
698  
699  
700  
701  
702  
703  
704  
705  
706  
707  
708  
709  
710  
711  
712  
713  
714  
715  
716  
717  
718  
719  
720  
721  
722  
723  
724  
725  
726  
727  
728  
729  
730  
731  
732  
733  
734  
735  
736  
737  
738  
739  
740  
741  
742  
743  
744  
745  
746  
747  
748  
749  
750  
751  
752  
753  
754  
755  
756  
757  
758  
759  
760  
761  
762  
763  
764  
765  
766  
767  
768  
769  
770  
771  
772  
773  
774  
775  
776  
777  
778  
779  
780  
781  
782  
783  
784  
785  
786  
787  
788  
789  
790  
791  
792  
793  
794  
795  
796  
797  
798  
799  
800  
801  
802  
803  
804  
805  
806  
807  
808  
809  
810  
811  
812  
813  
814  
815  
816  
817  
818  
819  
820  
821  
822  
823  
824  
825  
826  
827  
828  
829  
830  
831  
832  
833  
834  
835  
836  
837  
838  
839  
840  
841  
842  
843  
844  
845  
846  
847  
848  
849  
850  
851  
852  
853  
854  
855  
856  
857  
858  
859  
860  
861  
862  
863  
864  
865  
866  
867  
868  
869  
870  
871  
872  
873  
874  
875  
876  
877  
878  
879  
880  
881  
882  
883  
884  
885  
886  
887  
888  
889  
890  
891  
892  
893  
894  
895  
896  
897  
898  
899  
900  
901  
902  
903  
904  
905  
906  
907  
908  
909  
910  
911  
912  
913  
914  
915  
916  
917  
918  
919  
920  
921  
922  
923  
924  
925  
926  
927  
928  
929  
930  
931  
932  
933  
934  
935  
936  
937  
938  
939  
940  
941  
942  
943  
944  
945  
946  
947  
948  
949  
950  
951  
952  
953  
954  
955  
956  
957  
958  
959  
960  
961  
962  
963  
964  
965  
966  
967  
968  
969  
970  
971  
972  
973  
974  
975  
976  
977  
978  
979  
980  
981  
982  
983  
984  
985  
986  
987  
988  
989  
990  
991  
992  
993  
994  
995  
996  
997  
998  
999  
1000

1  
2  
3 421 pared output from MetUM-GA3 at N216 (90-km) and N512 (40-km), MRI-AGCM3-2H  
4  
5 422 (60-km) and MRI-AGCM3-2S (20-km), and GFDL-HiRAM-C180 (65-km) and GFDL-  
6  
7 423 HiRAM-C360 (32-km). We found consistent and inconsistent responses across the three  
8  
9 424 AGCMs to increasing resolution.

10  
11  
12 425 A summary plot about the model responses to horizontal resolution is presented in  
13  
14 426 Fig.11. All low-resolution AGCMs are biased toward higher annual mean precipitation and  
15  
16 427 stronger solstitial and equinoctial asymmetric modes. With increasing resolution, all  
17  
18 428 AGCMs show consistent improvements in simulating the precipitation and low-level circu-  
19  
20 429 lation of the annual mean and the first two annual cycle modes, as determined from the pat-  
21  
22 430 tern correlation coefficient and ETS as denoted by red boxes in Fig.11. Regionally, higher  
23  
24 431 pattern correlation coefficients are found in three high-resolution AGCMs for precipitation  
25  
26 432 for the annual mean (ANN), solstitial mode (AC1) and the equinoctial asymmetric mode  
27  
28 433 (AC2) for all regional monsoons, except the Australian (Aus) and North American mon-  
29  
30 434 soons (NAm). The inconsistent response to increased resolution across the three AGCMs  
31  
32 435 over North American and Australian monsoons may be partly due to their small monsoon  
33  
34 436 area.

35  
36  
37  
38  
39 437 We found that improvements in simulating the summer monsoon onset and withdrawal  
40  
41 438 are regionally dependent. No consistent response to resolution is found in simulating mon-  
42  
43 439 soon withdrawal. A consistent improvement in simulating East Asian (EAs), Southeast  
44  
45 440 Asian (SAs) and Western African (Waf) monsoon onset are shown across three AGCMs,  
46  
47 441 by delaying the monsoon onset over EAs and Waf and advancing over SAs. A consistent-  
48  
49 442 ly weakened equinoctial asymmetric mode over EAs and Waf with increasing resolution is  
50  
51 443 seen across the three models, reducing wet biases in the transition seasons. Thus, the sum-  
52  
53 444 mer monsoon onset pentad of the two regional monsoons is systematically delayed in all  
54  
55 445 high-resolution models relative to their low-resolution counterparts. In contrast, the im-  
56  
57  
58  
59  
60

1  
2  
3 446 improvements of monsoon onset over SAs are consistently advanced across three models.  
4  
5 447 Systematic errors and responses to resolution differ greatly across the three AGCMs for the  
6  
7  
8 448 simulated Indian (India) North American (NA) and South hemispheric regional mon-  
9  
10 449 soons (Aus, SAf, SAm), and the response to resolution differs across the three AGCM, in-  
11  
12 450 dicating the dependence of these regions on physical parameterizations. Nevertheless,  
13  
14 451 better representation on the Indian are shown in all three AGCMs.

15  
16  
17 452 Comparing the impact of resolution on the simulated regional monsoon precipitation  
18  
19 453 annual cycle, this study demonstrates the importance of resolution for the East Asian mon-  
20  
21 454 soon and West African monsoon where improved annual cycles are simulated in the three  
22  
23 455 AGCMs. The positive bias of AC2 over the West African monsoon region is caused by  
24  
25 456 overestimated precipitation in spring; in CMIP5 models, this bias has been linked to the  
26  
27 457 representation of African Easterly Waves (see Fig.6 in Martin and Thorncroft 2015). Both  
28  
29 458 the AMIP and historical simulations of CMIP5 show wet biases over northern Africa in  
30  
31 459 spring; this bias is significantly reduced in high-resolution models. A possible reason is  
32  
33 460 that the finer resolution weakens the excessive African Easterly wave activity over  
34  
35 461 northern Africa and thus reduces rainfall (Martin and Thorncroft 2015). Over the East  
36  
37 462 Asian monsoon region, the summer monsoon rainfall, particularly the Meiyu-Baiyu rain-  
38  
39 463 belt, is underestimated in many contemporary models (Kang 2004; Huang et al. 2013).  
40  
41 464 Therefore, the simulated contribution of summer rainfall to the annual total is also underes-  
42  
43 465 timated, resulting in relatively faster fractional accumulations of precipitation in spring and  
44  
45 466 earlier onset of EAs. As shown in Yao et al. (2017), as resolution increases, intensified nor-  
46  
47 467 therly flow over the central northern areas of China and southerly flow to the south of  
48  
49 468 Japan is found both from the AMIP simulations in CMIP5 and in CAM5 with different  
50  
51 469 resolutions. Those changes with resolution are related to the topography driven barotropic  
52  
53 470 Rossby waves downstream of the Tibetan Plateau (Yao et al. 2017). However, how the in-  
54  
55  
56  
57  
58  
59  
60

1  
2  
3 471 creased resolution affects the regional circulation remains inconclusive and deserves fur-  
4  
5 472 ther investigation.  
6

7  
8 473 Although several consistent responses to resolution are identified across the three  
9  
10 474 AGCMs considered, large differences still exist, especially over the Indian monsoon re-  
11  
12 475 gion. Large differences in the sensitivity to resolution over the Indian monsoon region  
13  
14 476 were found between MetUM-GA3 and MRI-AGCM3, particularly in synoptic and intra-  
15  
16 477 seasonal variability, such as monsoon low-pressure systems (Ogata et al. 2017). Those in-  
17  
18 478 consistencies across models demonstrate the importance of improving physical parameteri-  
19  
20 479 zations to reduce these systematic errors. This paper highlights the need for further multi-  
21  
22 480 model comparisons to determine the added value of horizontal resolution in climate simu-  
23  
24 481 lations.  
25  
26  
27  
28  
29  
30

### 31 483 **Acknowledgements:**

32  
33  
34 484 This work was jointly supported by the National Natural Science Foundation of China  
35  
36 485 under grant Nos. 41420104006 and 41330423, Program of International S&T Cooperation  
37  
38 486 under grant 2016YFE0102400, and the UK-China Research & Innovation Partnership  
39  
40 487 Fund through the Met Office Climate Science for Service Partnership (CSSP) China as part  
41  
42 488 of the Newton Fund. Nicholas P. Klingaman was funded by an Independent Research  
43  
44 489 Fellowship from the Natural Environment Research Council (NE/L010976/1).  
45  
46  
47  
48  
49  
50  
51  
52  
53  
54  
55  
56  
57  
58  
59  
60

490 **References:**

- 491 Adler, R. et al. 2003: The version-2 global precipitation climatology project (GPCP)  
492 monthly precipitation analysis (1979-present). *J. Hydrometeorol.* 4, 1147-1167.
- 493 Berckmans Julie, Tim Woollings, Marie-Estelle Demory, Pier-Luigi Vlidale, and Malcolm  
494 Robserts, 2013: Atmospheric blocking in a high resolution climate model: influences of  
495 mean state, orography and eddy forcing, *Atmos. Sci. Let.* **14**: 34–40.
- 496 Chen J.H, S. J. Lin, 2012: Seasonal Predictions of Tropical Cyclones Using a 25-km-  
497 Resolution General Circulation Model, *Journal of Climate.* **26**:380-398.
- 498 Dong G., H. Zhang, A. Moise, L. Hanson, P. Liang, H. Ye, 2016: CMIP5 model-simulated  
499 onset, duration and intensity of the Asian summer monsoon in current and future  
500 climate. *Clim Dyn.*, **46**:355–382. DOI 10.1007/s00382-015-2588-z
- 501 Donlon C. J., Martin M., Stark J., Roberts-Jones J., Fiedler E., and Wimmer W. 2012. The  
502 Operational Sea Surface Temperature and Sea Ice Analysis (OSTIA) system, *Remote*  
503 *Sens. Environ.*, **116**, 140-158, doi:10.1016/j.rse.2010.10.017.
- 504 Endo H, Kitoh A, Ose T, Mizuta R, Kusunoki S (2012) Future changes and uncertainties in  
505 Asian precipitation simulated by multiphysics and multi-sea surface temperature  
506 ensemble experiments with high-resolution Meteorological Research Institute  
507 atmospheric general circulation models (MRI-AGCMs). *J Geophys Res* 117:D16118.  
508 doi:10.1029/2012JD017874
- 509 Higgins R. W., and W. Shi, 2001: Intercomparison of the principal modes of interannual  
510 and intraseasonal variability of the North American Monsoon System. *J. Climate*, **14**,  
511 403-417.
- 512 Huang, D. Q., J. Zhu, Y.-C. Zhang, and A.-N. Huang, 2013: Uncertainties on the simulated



- 1  
2  
3 513 summer precipitation over eastern China from the CMIP5 models. *J. Geophys. Res.*  
4  
5 514 *Atmos.*, 118, 9035–9047  
6  
7  
8  
9 515 Huffman G. J., D. T. Bolvin, E. J. Nelkin, D. B. Wolff, R. F. Adler, G. Gu, Y. Hong, K. P.  
10  
11 516 Bowman, and E. F. Stocker. 2007: The TRMM multisatellite precipitation analysis  
12  
13 517 (TMPA): Quasi-global, multiyear, combined-sensor precipitation estimates at fine  
14  
15 518 scales, *J. Hydrometeorol.*, **8(1)**: 38-55.  
16  
17  
18 519 Hung C.W, M. Yanai, 2004: Factors contributing to the Australian summer monsoon.  
19  
20 520 *Q.J.R. Meteorol. Soc.*, **130**: 739-758.  
21  
22  
23 521 Johnson SJ et al 2016: The resolution sensitivity of the South Asian monsoon and Indo-  
24  
25 522 Pacific in a global 0.35° AGCM. *Clim Dyn.*, **46(3)**: 807–831  
26  
27  
28  
29 523 Jolliffe, I.T., and D.B. Stephenson, 2003: Forecast Verification: A Practitioner's Guide in  
30  
31 524 Atmospheric Science. Wiley, Hoboken, NJ, 240 pp.  
32  
33  
34  
35 525 Kang, I.-S., 2004: Current status of AGCM monsoon simulations. East Asian Monsoon,  
36  
37 526 C.-P. Chang, Ed., World Scientific, 301–331.  
38  
39  
40 527 Kitoh A, Kusunoki S. 2008: East Asian summer monsoon simulation by a 20-km mesh  
41  
42 528 AGCM. *Climate Dyn.*, **31**: 389-401. doi:10.1007/s00382-007-0285-2.  
43  
44  
45 529 Krishnamurti TN, Ramanathan Y (1982) Sensitivity of the monsoon onset to differential  
46  
47 530 heating. *J Atmos Sci.* **39(6)**:1290–1306  
48  
49  
50  
51 531 Kusunoki Shoji, 2016: Is the global atmospheric model MRI-AGCM3.2 better than the  
52  
53 532 CMIP5 atmospheric models in simulating precipitation over East Asia, *Clim Dyn*, doi:  
54  
55 533 10.1007/s00382-016-3335-9.  
56  
57  
58  
59 534 Li, J., R. Yu, W. Yuan, H. Chen, W. Sun, Y. Zhang. 2015: Precipitation over East Asia

- 1  
2  
3 535 simulated by NCAR CAM5 at different horizontal resolutions. *Journal of Advances in*  
4  
5 536 *Modeling Earth Systems*, **7(2)**, 774-790. DOI 10.1002/2014MS000414  
6  
7  
8 537 Li P., T. Zhou, X. Chen, 2017: Water vapor transport for spring persistent rains over  
9  
10 538 southeastern China based on five reanalysis datasets. *Climate Dynamics*, DOI  
11  
12 10.1007/s00382-017-3680-3  
13  
14  
15 540 Liu Y. M., Chan J.C., Mao J. Y., Wu G. X., 2002: The role of Bay of Bengal convection in  
16  
17 541 the onset of the 1998 South China Sea summer monsoon. *Mon Weather Rev*, **130**: 2731–  
18  
19 542 2744  
20  
21  
22 543 Mao J.Y., Wu G.X., 2007: Interannual variability in the onset of the summer monsoon over  
23  
24 544 eastern Bay of Bengal. *Theor Appl Climatol.*, **89**:155–170  
25  
26  
27 545 Martin E. R., and C. Thorncroft, 2015: Representation of African Easterly Waves in  
28  
29 546 CMIP5 Models, *J. Climate*, **28**, 7702-7715.  
30  
31  
32 547 Mizielinski, M. S., M. J. Roberts, P. L. Vidale, R. Schiemann, M.-E. Demory, J. Strachan,  
33  
34 548 T. Edwards, A. Stephens, B. N. Lawrence, M. Pritchard, P. Chiu, A. Iwi, J. Churchill,  
35  
36 549 C. Del Cano Novales, J. Kettleborough, W. Roseblade, P. Selwood, M. Foster, M.  
37  
38 550 Glover, and A. Malcolm. 2014: High resolution global climate modelling; the  
39  
40 551 UPSCALE project, a large simulation campaign. *Geosci. Model Dev.*, **7**: 563-591.  
41  
42  
43 552 Mizuta R, Yoshimura H, Murakami H, Matsueda M, Endo H, Ose T, Kamiguchi K,  
44  
45 553 Hosaka M, Sugi M, Yukimoto S, Kusunoki S, Kitoh A. 2012: Climate simulations  
46  
47 554 using MRI-AGCM3.2 with 20-km grid. *J Meteor Soc Japan*, **90A**: 233-258.  
48  
49 555 doi:10.2151/jmsj.2012-A12  
50  
51  
52 556 Ogata T., S. J. Johnson, R. Shiemann, M. Demory, R. Mizuta, K. Yoshida, O. Arakawa,  
53  
54 557 2017: The resolution sensitivity of the Asian summer monsoon and its inter-model  
55  
56 558 comparison between MRI-AGCM and MetUM. *Clim Dyn*, DOI 10.1007/s00382-016-

- 1  
2  
3 559 3517-5  
4  
5  
6 560 Raia A., I. F. A. Cavalcanti, 2008: The life cycle of the South African monsoon system.  
7  
8 561 *Journal of Climate*, **21**: 6227-6246.  
9  
10  
11 562 Rayner, N. A.; Parker, D. E.; Horton, E. B.; Folland, C. K.; Alexander, L. V.; Rowell, D.  
12  
13 563 P.; Kent, E. C.; Kaplan, A., 2003: Global analyses of sea surface temperature, sea ice,  
14  
15 564 and night marine air temperature since the late nineteenth century *J. Geophys. Res.* **108**:  
16  
17 565 4407 10.1029/2002JD002670  
18  
19  
20  
21 566 Sperber KR, Annamalai H, Kang IS, Kitoh A, Moise A, Turner A, Wang B, Zhou T, 2013:  
22  
23 567 The Asian summer monsoon: an inter- comparison of CMIP5 vs. CMIP3 simulations of  
24  
25 568 the late 20th century. *Clim Dyn* **41**: 2711–2744  
26  
27  
28  
29 569 Sperber K R, Annamalai H, 2014: The use of fractional accumulated precipitation for the  
30  
31 570 evaluation of the annual cycle of monsoons. *Clim Dyn.*, **43**: 3219–3244 DOI  
32  
33 571 10.1007/s00382-014-2099-3  
34  
35  
36  
37 572 Sultan B., S. Janicot, 2003: The West African Monsoon Dynamics. Part II: The “Pre-  
38  
39 573 onset” and “Onset” of the Summer Monsoon. *Journal of Climate*, **16**: 3407-3427.  
40  
41  
42  
43 574 Trenberth K, Stepaniak D, and Caron J. 2000: The global monsoon as seen through the di-  
44  
45 575 vergent atmospheric circulation. *Journal of Climate*, **13(22)**: 3 969-3 993.  
46  
47  
48  
49 576 Wang B., H. Lin 2002: Rainy season of the Asian-Pacific summer monsoon. *J Clim.*, **15**:  
50  
51 577 386–398  
52  
53  
54 578 Wang B, Ding Q. 2008: Global monsoon: dominant mode of annual variation in the trop-  
55  
56 579 ics. *Dyn Atmos Oceans*, **44**:165–183. doi:10. 1016/j.dynatmoce.2007.05.002  
57  
58  
59 580 Wu G.X., Zhang Y.S. 1998: Tibetan Plateau forcing and the situating and timing of the

- 1  
2  
3 581 Asian monsoon onset. *Mon. Wea. Rev.*, **126**: 913–927  
4  
5  
6 582 Wu G. X., Guan Y., Liu Y.M., Yan J.H., Mao J.Y. 2012: Air–sea interaction and formation  
7  
8 583 of the Asian summer monsoon onset vortex over the Bay of Bengal. *Clim Dyn.*, **38**:  
9  
10 584 261–279.  
11  
12  
13  
14 585 Xu J., Chan J.C. 2001: First transition of the Asian summer monsoon in 1998 and the ef-  
15  
16 586 fect of the Tibet: tropical ocean thermal contrast. *J Meteor Soc Japan*, **79**: 241–253  
17  
18  
19  
20 587 Yao Junchen, Tianjun Zhou, Zhun Guo, Xiaolong Chen, Liwei Zou, Yong Sun, 2017: Im-  
21  
22 588 proved performance of High-Resolution Atmospheric Models in simulating the East-  
23  
24 589 Asian Summer Monsoon Rainbelt. *Journal of Climate*, in press.  
25  
26  
27  
28 590 Yu, B., and J. M. Wallace, 2000: The principal mode of interannual variability of the North  
29  
30 591 American Monsoon System. *J. Climate*, **13**, 2794-2800.  
31  
32  
33 592 Zhang L., P. Wu, T. Zhou, M. Roberts, R. Schiemann, 2016: Added value of high resolu-  
34  
35 593 tion models in simulating global precipitation characteristics. *Atmospheric Science Let-*  
36  
37 594 *ters*, **17**: 646-657.  
38  
39  
40  
41 595 Zhao M., Isaac M. Held, Shian-Jiann Lin, and Gabriel A. Vecchi. 2009: Simulations of  
42  
43 596 Global Hurricane Climatology, Interannual Variability, and Response to Global Warm-  
44  
45 597 ing Using a 50-km Resolution GCM. *J. Climate*, **22**: 6653-6678. doi:  
46  
47 598 <http://dx.doi.org/10.1175/2009JCLI3049.1>  
48  
49  
50  
51 599 Zhou Tianjun, Xiaolong Chen, Bo Wu, Zhun Guo, Yong Sun, Liwei Zou, Wenmin Man,  
52  
53 600 Lixia Zhang, Chao He, 2017: A Robustness Analysis of CMIP5 Models over the East  
54  
55 601 Asia-Western North Pacific Domain, *Engineering*, 3(5), 773-778,  
56  
57 602 <https://doi.org/10.1016/J.ENG.2017.05.018>  
58  
59  
60

1  
2  
3 603 Zou, L. W., and T. J. Zhou, 2015: Asian summer monsoon onset in simulations and CMIP5  
4  
5 604 projections using four Chinese climate models. *Adv. Atmos. Sci.*, **32(6)**: 794-806.  
6  
7  
8  
9 605  
10  
11  
12  
13  
14  
15  
16  
17  
18  
19  
20  
21  
22  
23  
24  
25  
26  
27  
28  
29  
30  
31  
32  
33  
34  
35  
36  
37  
38  
39  
40  
41  
42  
43  
44  
45  
46  
47  
48  
49  
50  
51  
52  
53  
54  
55  
56  
57  
58  
59  
60

For Review Only

1  
2  
3 **606 Figure Captions:**  
4  
5

6 **607 Table 1** Model descriptions including model resolution, sea surface temperature (SST)  
7  
8 forcing, realization numbers and selected simulation years.  
9

10 **609 Table 2.** Schematic contingency table for computing the ETS metric for model simulations  
11  
12 of the monsoon domain (after Table 3.1 in Jolliffe and Stephenson 2003)  
13  
14

15 **611 Figure 1** Spatial distributions of the difference between low-resolution models and TRMM  
16  
17 (units:  $\text{mm day}^{-1}$ , left column) and between high and low resolutions of the same model  
18  
19 (units:  $\text{mm day}^{-1}$ , right column) in simulating annual mean precipitation. (a) MetUM-  
20  
21 GA3 N216 minus TRMM, (b) MetUM-GA3 N512 minus MetUM-GA3 N216, (c) MRI-  
22  
23 AGCM3-2H minus TRMM, (d) MRI-AGCM3-2S minus MRI-AGCM3-2H, (e) GFDL-  
24  
25 AGCM3-2H minus TRMM, (f) GFDL-HiRAM-C360 minus GFDL-HiRAM-C180.  
26  
27 Blue lines in the left and right columns show the climatological mean precipitation from  
28  
29 TRMM and the low-resolution models, respectively. The hatched area denotes where  
30  
31 precipitation exceeds  $7\text{mm day}^{-1}$ .  
32  
33  
34  
35

36 **620 Figure 2** As in Figure 1, but for the spatial distribution of the solstitial mode (unit:  $\text{mm}$   
37  
38  $\text{day}^{-1}$ ), defined as the difference between June-September (JJAS) and December-March  
39  
40 (DJFM) mean precipitation. The blue and red lines indicate positive and negative val-  
41  
42 ues, respectively.  
43  
44

45 **624 Figure 3** As in Figure 1, but for the equinoctial asymmetric mode defined as the difference  
46  
47 between April-May (AM) and October-November (ON) mean precipitation.  
48  
49

50 **626 Figure 4** Scatter diagrams for the fidelity of simulated precipitation and 850hPa winds of  
51  
52 (a)-(c) annual mean, (d)-(f) solstitial mode, and (g)-(i) equinoctial asymmetric mode  
53  
54 against TRMM and CFSR. The abscissa and ordinate are the pattern correlation coeffi-  
55  
56 cients (PCC) and root-mean-square-error (RMSE), respectively. The fidelity of GPCP  
57  
58 and NCEP2 against TRMM and CFSR are also shown in dots to represent the observa-  
59  
60

631 tional uncertainty. The stars, triangles and diamonds represent the results from MetUM-  
 632 GA3, MRI-AGCM3 and GFDL-HiRAM, respectively, with high-resolution models in  
 633 red and low-resolution in blue.

634 **Figure 5** Climatological annual range of precipitation (shaded, units: mm day<sup>-1</sup>) and glob-  
 635 al monsoon domain (contours) derived from (a) TRMM, (b) GPCP, (c) MetUM-GA3  
 636 N216, (d) MetUM-GA3 N512, (e) MRI-AGCM3-2H, (f) MRI-AGCM3-2S, (g) GFDL-  
 637 HiRAM-C180, (h) GFDL-HiRAM-C360. The annual range is defined as the May to  
 638 September (MJJAS) minus November to March (NDJFM) mean precipitation for the  
 639 Northern Hemisphere, and NDJFM minus MJJAS for the Southern Hemisphere.

640 **Figure 6.** The ETS score of monsoon domain simulation over (a) global (GM), (b) Indian  
 641 (India), (c) Southeast Asia (SAs), (d) East Asian (EAs), (e) Australian (Aus), (f) West  
 642 African (Waf), (g) South African (SAf), (h) North American (NAm) and (i) South  
 643 American (SAm) monsoon. The abscissa (ordinate) is ETS scores of simulated domain  
 644 derived from precipitation (U850), respectively. The fidelity of GPCP against TRMM is  
 645 shown in dots. The fidelity of GPCP and NCEP2 against TRMM and CFSR are also  
 646 shown in dots to represent the observational uncertainty. The star, triangle and diamond  
 647 represent the results from MetUM-GA3, MRI-AGCM3 and GFDL-HiRAM, respective-  
 648 ly, with high-resolution models in red and low-resolution in blue.

649 **Figure 7** Observed and simulated precipitation accumulations (unit: mm) from the first  
 650 pentad to the end of year, and fractional accumulations (unit: %) around the monsoon  
 651 onset pentad averaged over (a) Indian (India), (b) Southeast Asian (SAs), (c) East Asian  
 652 (EAs), (d) Australian (Aus), (e) West African (Waf), (f) South African (SAf), (g) North  
 653 American (NAm) and (h) South American (SAm) monsoon. Note: for Southern Hemi-  
 654 sphere locations (Australian, South African, and South American monsoons) the pen-  
 655 tads were reordered to July–June prior to the analysis. The black, red, blue and green

1  
2  
3 656 lines represent the results of TRMM, MetUM-GA3, MRI-AGCM3 and GFDL-HiRAM,  
4  
5 657 respectively, with high-resolution configurations in solid lines and low-resolution con-  
6  
7 658 figurations in dashed lines.

9  
10 659 **Figure 8** Climatological monsoon onset pentad derived from (a) TRMM, (b) GPCP, (c)  
11  
12 660 MetUM-GA3 N216, (d) MetUM-GA3 N512, (e) MRI-AGCM3-2H, (f) MRI-AGCM3-  
13  
14 661 2S, (g) GFDL-HiRAM-C180, (h) GFDL-HiRAM-C360. The monsoon onset pentad is  
15  
16 662 defined as the pentad when fractional accumulation first becomes  $\geq 0.2$  (Sperber and  
17  
18 663 Annamalai 2014). Note: for Southern Hemisphere locations (Australian, South African,  
19  
20 664 and South American monsoon) the pentads were reordered to July–June prior to the  
21  
22 665 analysis.

23  
24  
25  
26 666 **Figure 9** As in Figure 8, but for the monsoon withdrawal pentad, defined as the pentad  
27  
28 667 with fractional accumulation first becomes  $\geq 0.8$  (Sperber and Annamalai 2014). Note:  
29  
30 668 for Southern Hemisphere locations (Australian, South African, and South American  
31  
32 669 monsoon) the pentads were reordered to July–June prior to the analysis.

33  
34  
35 670 **Figure 10** The monsoon onset (x axis) and withdraw pentad (y axis) averaged over (a) In-  
36  
37 671 dian (India), (b) Southeast Asian (SAs), (c) East Asian (EAs), (d) Australian (Aus), (e)  
38  
39 672 West African (Waf), (f) South African (SAf), (g) North American (NAf) and (h)  
40  
41 673 South American (SAm) monsoon. Note: for Southern Hemisphere locations (Australian,  
42  
43 674 South African, and South American monsoon) the pentads were reordered to July–June  
44  
45 675 prior to the analysis. The dots, stars, triangles and diamonds represent the results from  
46  
47 676 the observations, MetUM-GA3, MRI-AGCM3 and GFDL-HiRAM, respectively, with  
48  
49 677 high-resolution configurations in red and low-resolution configurations in blue.

50  
51  
52  
53 678 **Figure 11** Improvement of the simulation on the annual cycle of global monsoon precipita-  
54  
55 679 tion with horizontal resolution. Red boxes indicate high-resolution consistently im-  
56  
57 680 proves performance across all three AGCMs; blue boxes indicate improvements with  
58  
59  
60



1  
2  
3 681 resolution are inconsistent; orange boxes indicate a better simulation is shown in all  
4  
5 682 three high-resolution AGCMs but the responses to resolution are inconsistent across  
6  
7  
8 683 models. The values from left to right in each box are the difference between high- and  
9  
10 684 low-resolution configurations of MetUM-GA3, MRI-AGCM3 and GFDL-HiRAM, re-  
11  
12 685 spectively. The metric for the annual modes, including annual mean (ANN), solstitial  
13  
14 686 mode (AC1), the equinoctial asymmetric mode (AC2), is the pattern correlation coeffi-  
15  
16 687 cient with TRMM. The metrics for the monsoon domain and monsoon onset/withdrawal  
17  
18  
19 688 are ETS and the onset/withdrawal pentad, respectively.  
20  
21  
22 689  
23  
24 690  
25  
26  
27 691  
28  
29  
30 692  
31  
32  
33  
34 693  
35  
36  
37  
38  
39  
40  
41  
42  
43  
44  
45  
46  
47  
48  
49  
50  
51  
52  
53  
54  
55  
56  
57  
58  
59  
60

694 **Table 1. Model information description including model resolution, sea surface tem-**  
 695 **perature (SST) forcing, realization numbers and selected simulation years.**

Model	Resolution	SST	Realiza- tions	Selected Years
MetUM-GA3	N216 (0.83°x0.55°)	OSTIA	3	1998-2008
	N512 (0.35°x0.23°)	OSTIA	5	1998-2008
GFDL- HiRAM	C180(0.625°x0.5°)	HadISST1	3	1998-2008
	C360(0.31°x0.25°)	HadISST1	2	1998-2008
MRI-AGCM3	2H(0.56°x0.56°)	HadISST1	2	1998-2008
	2S(0.18°x0.18°)	HadISST1	1	1998-2008

696  
 697  
 698

699 **Table 2. Schematic contingency table for computing the ETS metric for model**  
 700 **simulations of the monsoon domain (after Table 3.1 in Jolliffe and Stephenson 2003)**

	Event Observed		
Event Simulated	Monsoon domain	Non-monsoon domain	Total
Monsoon domain	a (Hits)	b (False alarms)	a+b
Non-monsoon domain	c (Misses)	d (Correct rejections)	c+d
Total	a+c	b+d	a+b+c+d=n

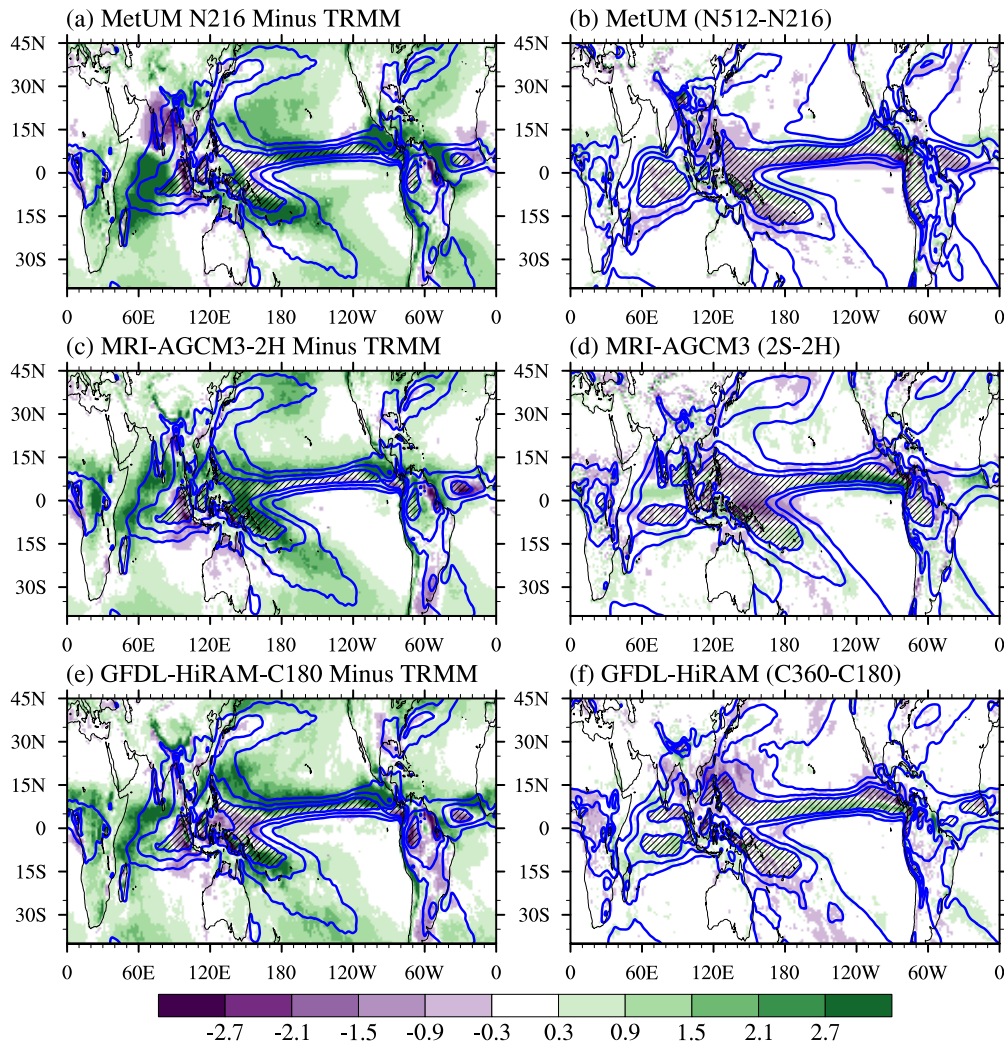
701

702

703

704

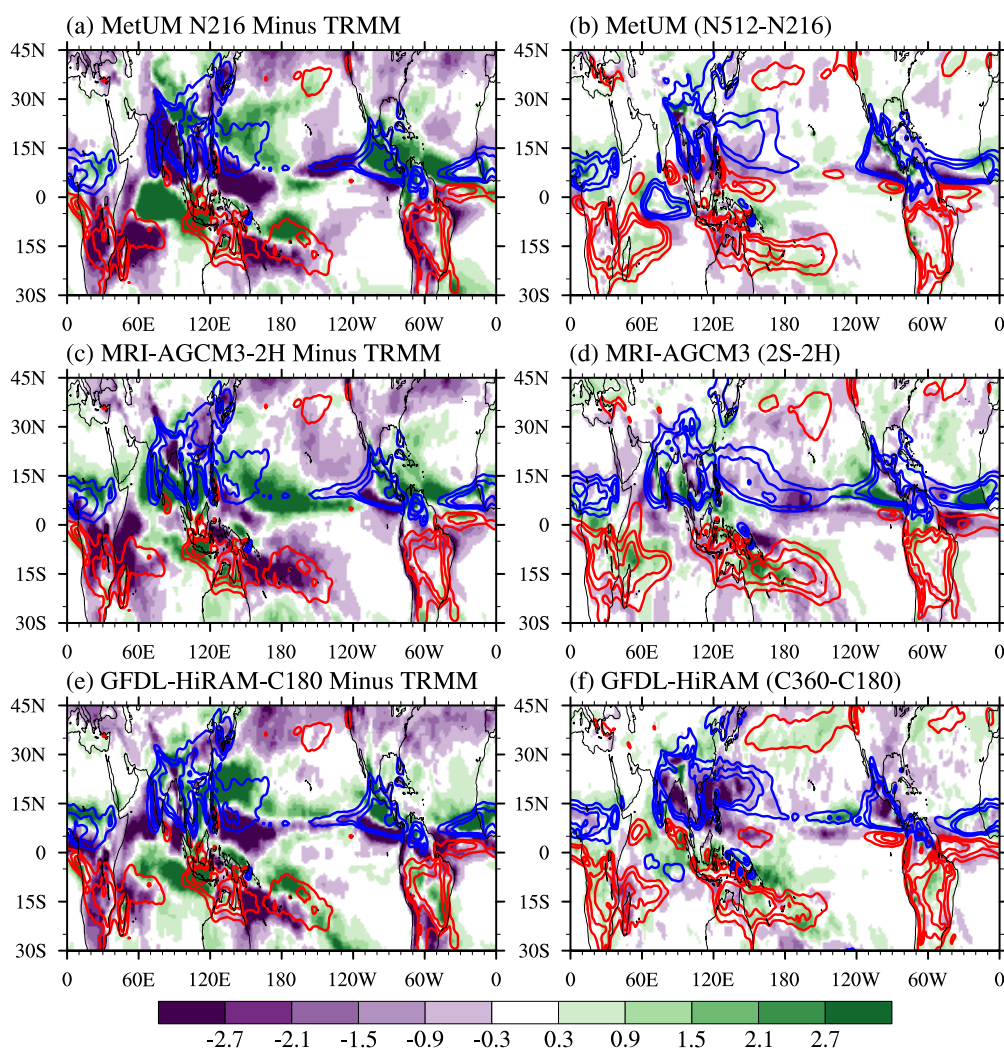
For Review Only



705

706 **Figure 1** Spatial distributions of the difference between low-resolution models and TRMM  
 707 (units: mm day<sup>-1</sup>, left column) and between high and low resolutions of the same model  
 708 (units: mm day<sup>-1</sup>, right column) in simulating annual mean precipitation. (a) MetUM-GA3  
 709 N216 minus TRMM, (b) MetUM-GA3 N512 minus MetUM-GA3 N216, (c) MRI-  
 710 AGCM3-2H minus TRMM, (d) MRI-AGCM3-2S minus MRI-AGCM3-2H, (e) GFDL-  
 711 HiRAM-C180 minus TRMM, (f) GFDL-HiRAM-C360 minus GFDL-HiRAM-C180. Blue  
 712 lines in the left and right columns show the climatological mean precipitation from TRMM  
 713 and the low-resolution models, respectively. The hatched area denotes where precipitation  
 714 exceeds 7mm day<sup>-1</sup>.

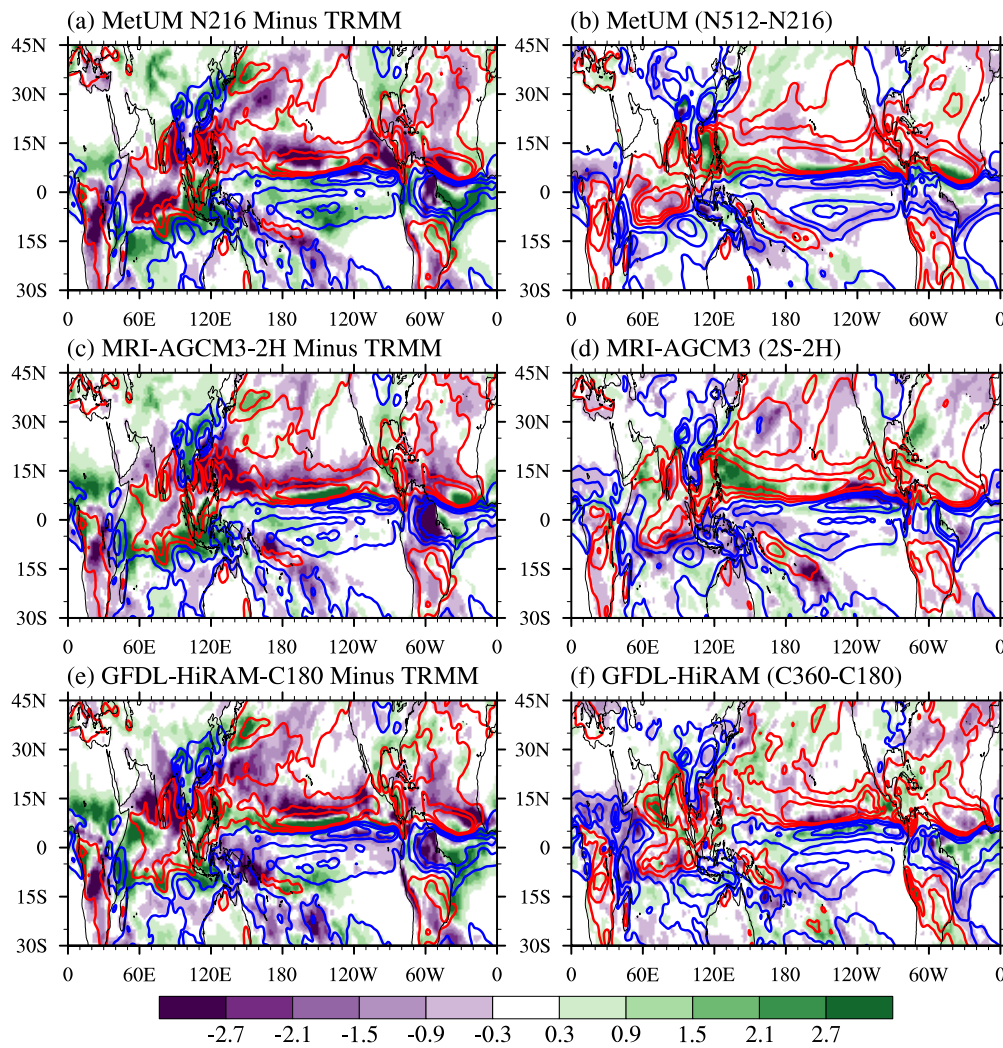
715



716

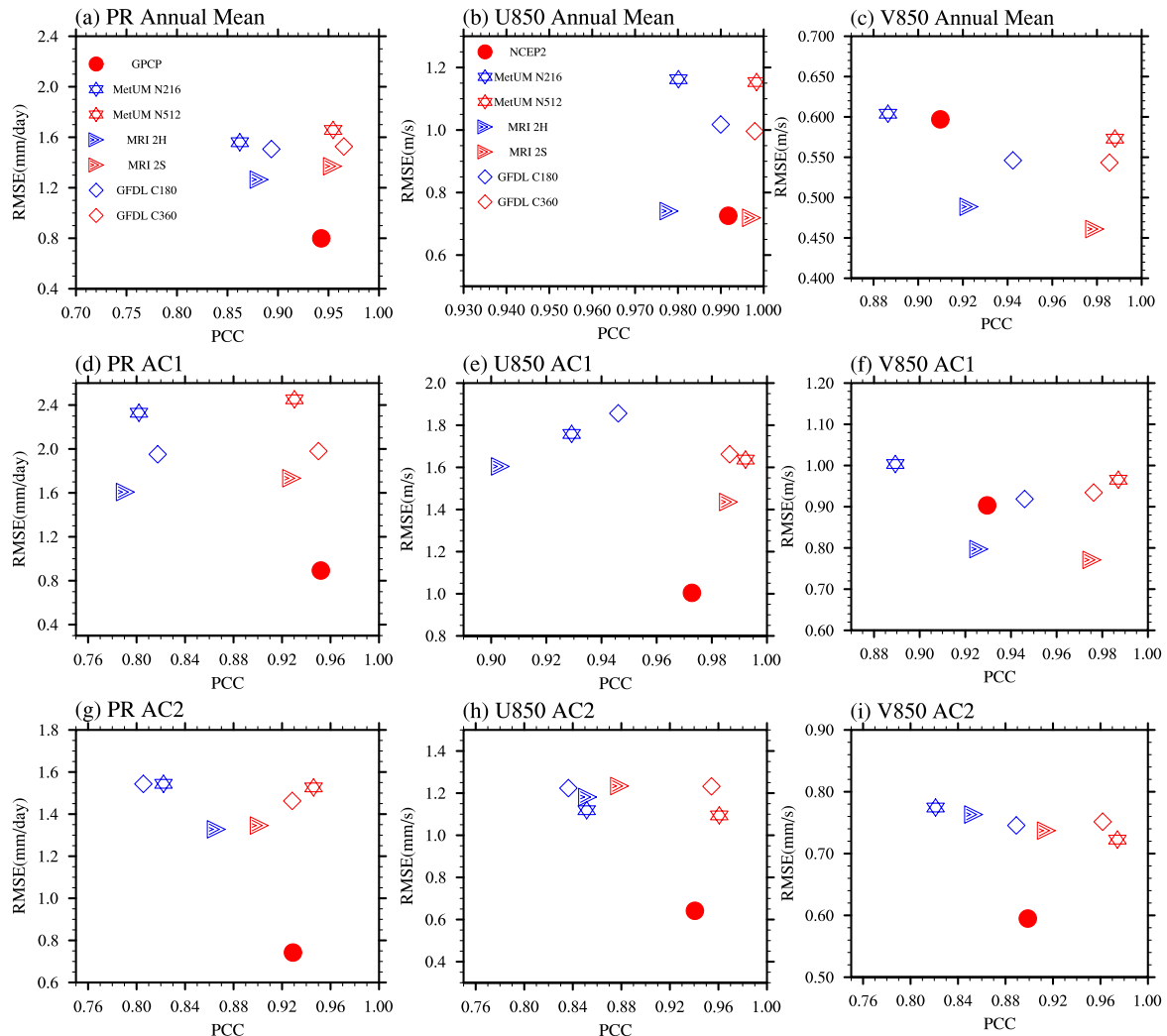
717 **Figure 2** As in Figure 1, but for the spatial distribution of the solstitial mode (unit: mm  
 718 day<sup>-1</sup>), defined as the difference between June-September (JJAS) and December-March  
 719 (DJFM) mean precipitation. The blue and red lines indicate positive and negative values,  
 720 respectively.

721



722

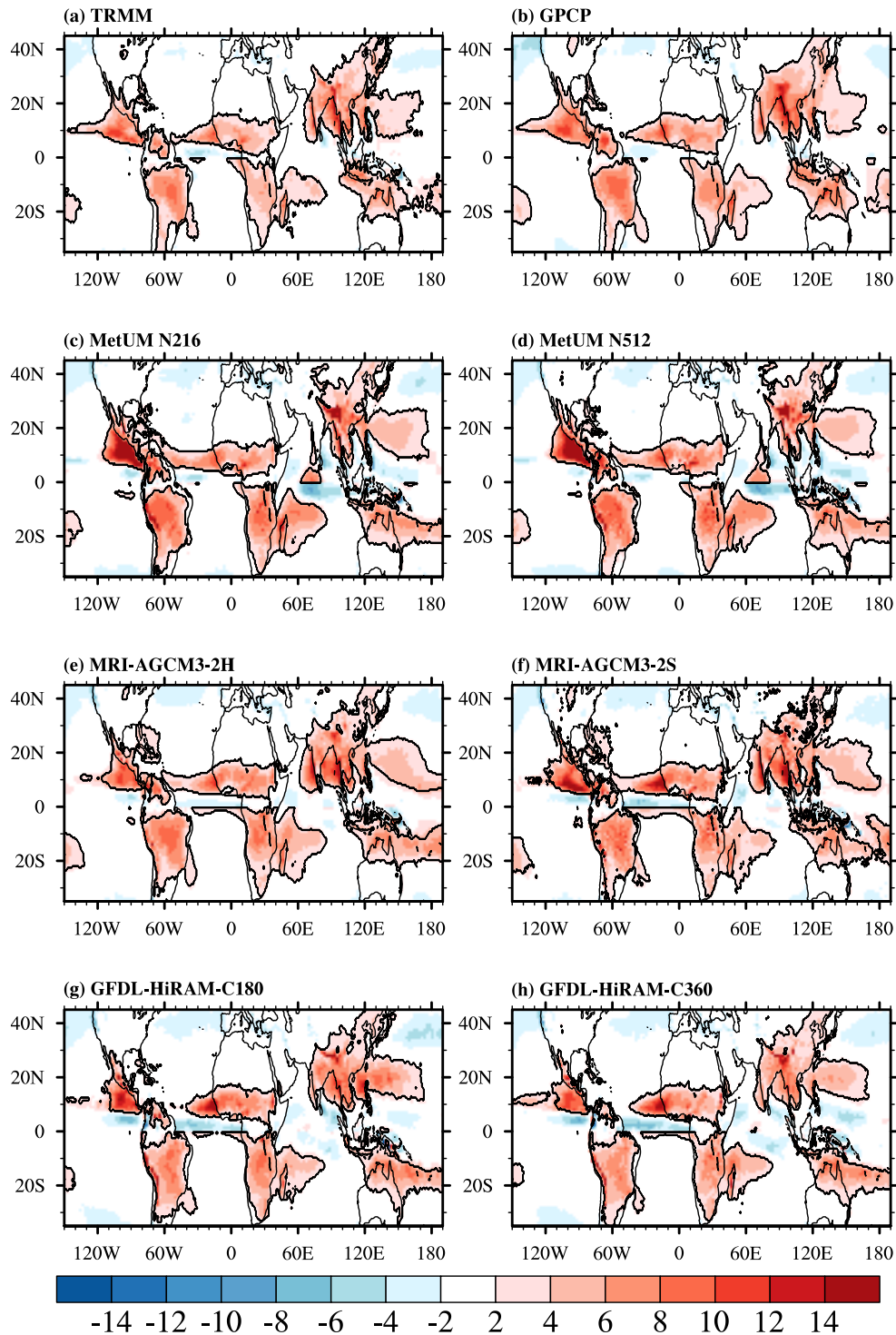
723 **Figure 3.** As in Figure 1, but for the equinoctial asymmetric mode defined as the differ-  
 724 ence between April-May (AM) and October-November (ON) mean precipitation.



725

726 **Figure 4** Scatter diagrams for the fidelity of simulated precipitation and 850hPa winds of  
 727 (a)-(c) annual mean, (d)-(f) solstitial mode, and (g)-(i) equinoctial asymmetric mode  
 728 against TRMM and CFSR. The abscissa and ordinate are the pattern correlation coefficients (PCC) and root-mean-square-error (RMSE), respectively. The fidelity of GPCP and  
 729 NCEP2 against TRMM and CFSR are also shown in dots to represent the observational  
 730 uncertainty. The stars, triangles and diamonds represent the results from MetUM-GA3,  
 731 MRI-AGCM3 and GFDL-HiRAM, respectively, with high-resolution configurations in red  
 732 and low-resolution configurations in blue.

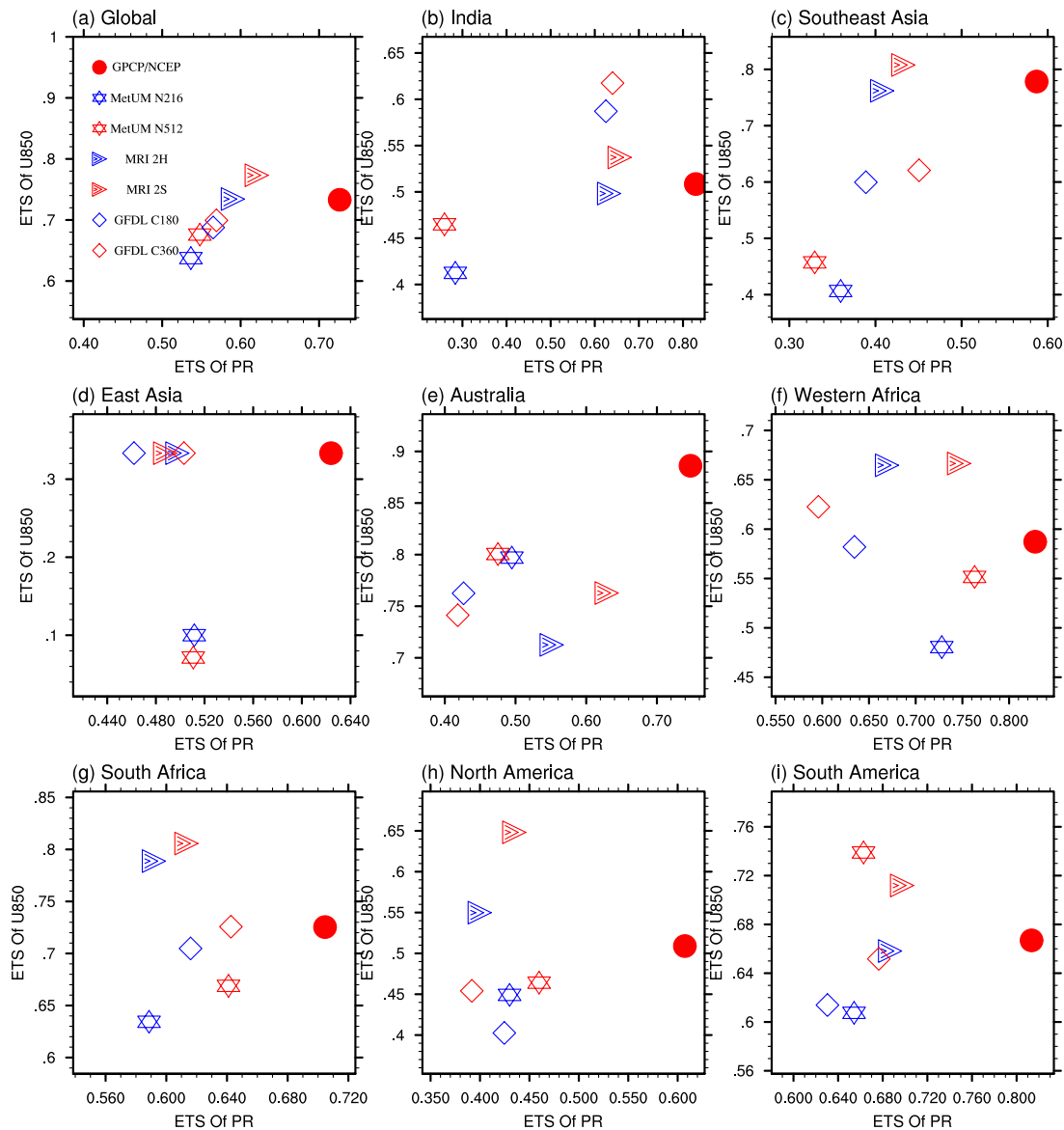
734



735

736 **Figure 5** Climatological annual range of precipitation (shaded, units: mm day<sup>-1</sup>) and glob-  
 737 al monsoon domain (contours) derived from (a) TRMM, (b) GPCP, (c) MetUM-GA3  
 738 N216, (d) MetUM-GA3 N512, (e) MRI-AGCM3-2H, (f) MRI-AGCM3-2S, (g) GFDL-  
 739 HiRAM-C180, (h) GFDL-HiRAM-C360. The annual range is defined as the May to Sep-  
 740 tember (MJJAS) minus November to March (NDJFM) mean precipitation for the Northern  
 741 Hemisphere, and NDJFM minus MJJAS for the Southern Hemisphere.





742

743 **Figure 6.** The ETS score of monsoon domain simulation over (a) global (GM), (b) Indian  
 744 (India), (c) Southeast Asian (SAs), (d) East Asian (EAs), (e) Australian (Aus), (f) West Af-  
 745 rican (Waf), (g) South African (SAf), (h) North American (NAm) and (i) South American  
 746 (SAm) monsoon. The abscissa (ordinate) is ETS scores of simulated domain derived from  
 747 precipitation (U850). The fidelity of GPCP against TRMM is shown in dots. The fidelity of  
 748 GPCP and NCEP2 against TRMM and CFSR are also shown in dots to represent the ob-  
 749 servational uncertainty. The star, triangle and diamond represent the results from MetUM-  
 750 GA3, MRI-AGCM3 and GFDL-HiRAM, respectively, with high-resolution configurations  
 751 in red and low-resolution configurations in blue.

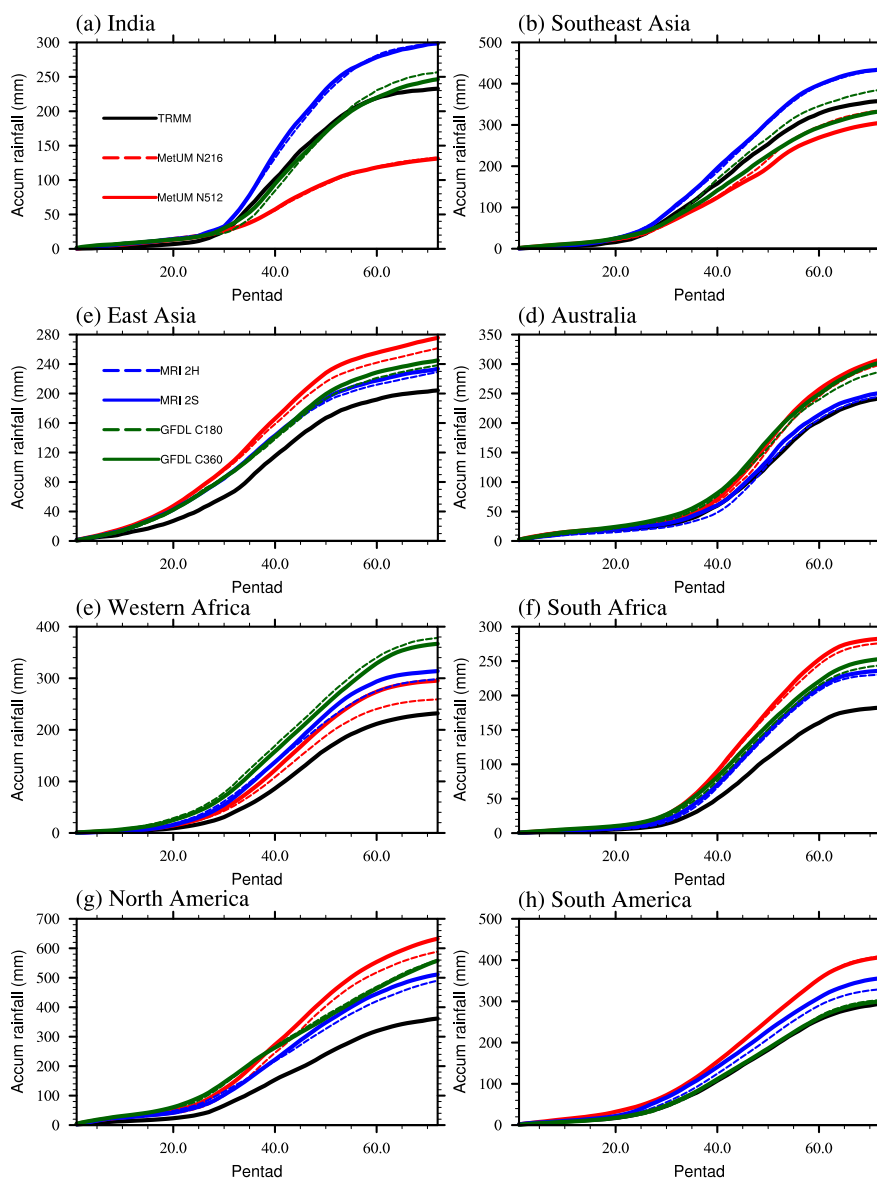


**Figure 7** Observed and simulated precipitation accumulations (unit: mm) from the first pentad to the end of year, and fractional accumulations (unit: %) around the monsoon onset pentad averaged over (a) Indian (India), (b) Southeast Asian (SAs), (c) East Asian (EAs), (d) Australian (Aus), (e) West African (Waf), (f) South African (SAf), (g) North American (NA<sub>m</sub>) and (h) South American (SA<sub>m</sub>) monsoon. Note: for Southern Hemisphere locations (Australian, South African, and South American monsoons) the pentads were reordered to July–June prior to the analysis. The black, red, blue and green lines represent the results of TRMM, MetUM-GA3, MRI-AGCM3 and GFDL-HiRAM, respectively, with high-resolution configurations in solid lines and low-resolution configurations in dashed lines.

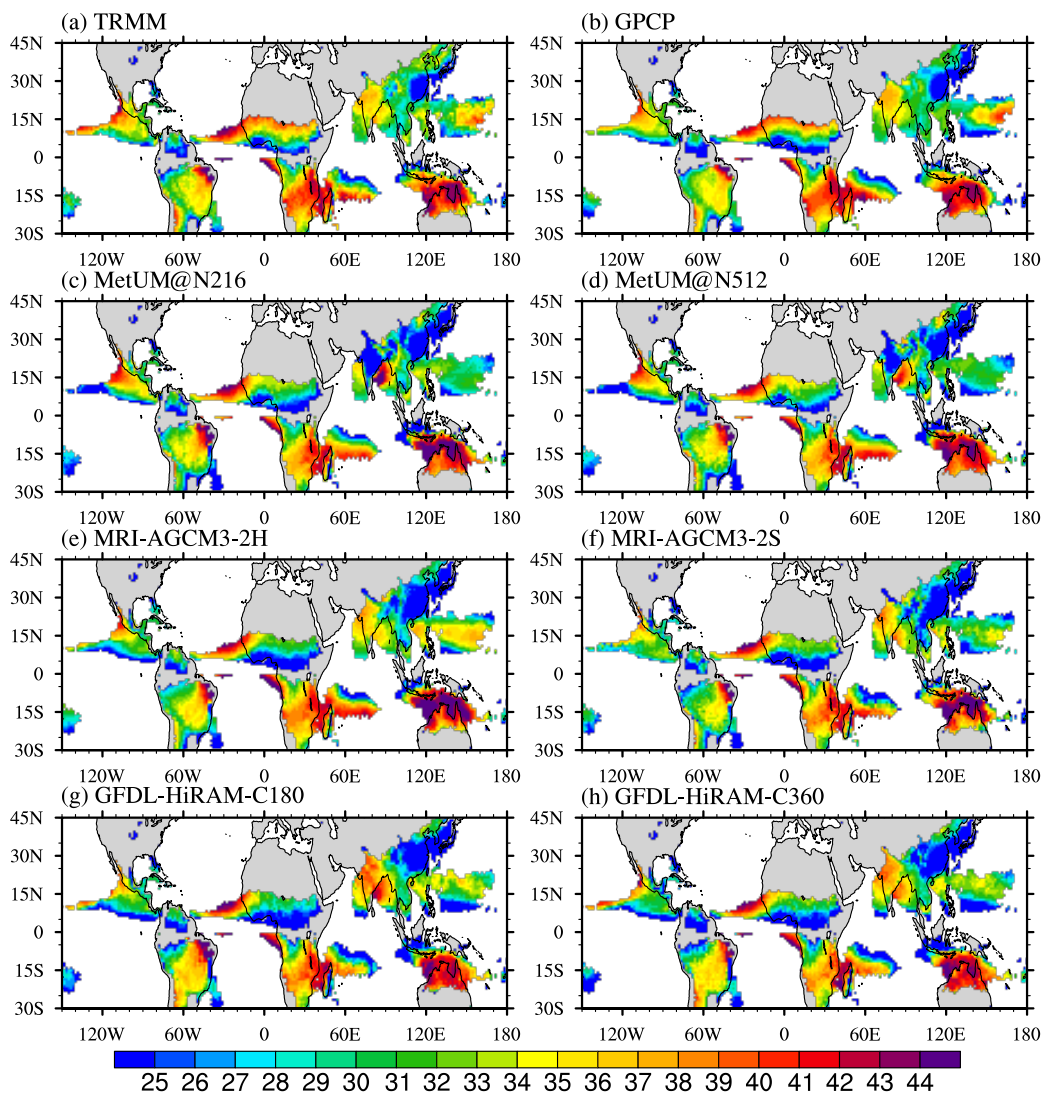


**Figure 8** Climatological monsoon onset pentad derived from (a) TRMM, (b) GPCP, (c) MetUM-GA3 N216, (d) MetUM-GA3 N512, (e) MRI-AGCM3-2H, (f) MRI-AGCM3-2S, (g) GFDL-HiRAM-C180, (h) GFDL-HiRAM-C360. The monsoon onset pentad is defined as the pentad when fractional accumulation first becomes  $\geq 0.2$  (Sperber and Annamalai 2014). Note: for Southern Hemisphere locations (Australian, South African, and South American monsoon) the pentads were reordered to July–June prior to the analysis.

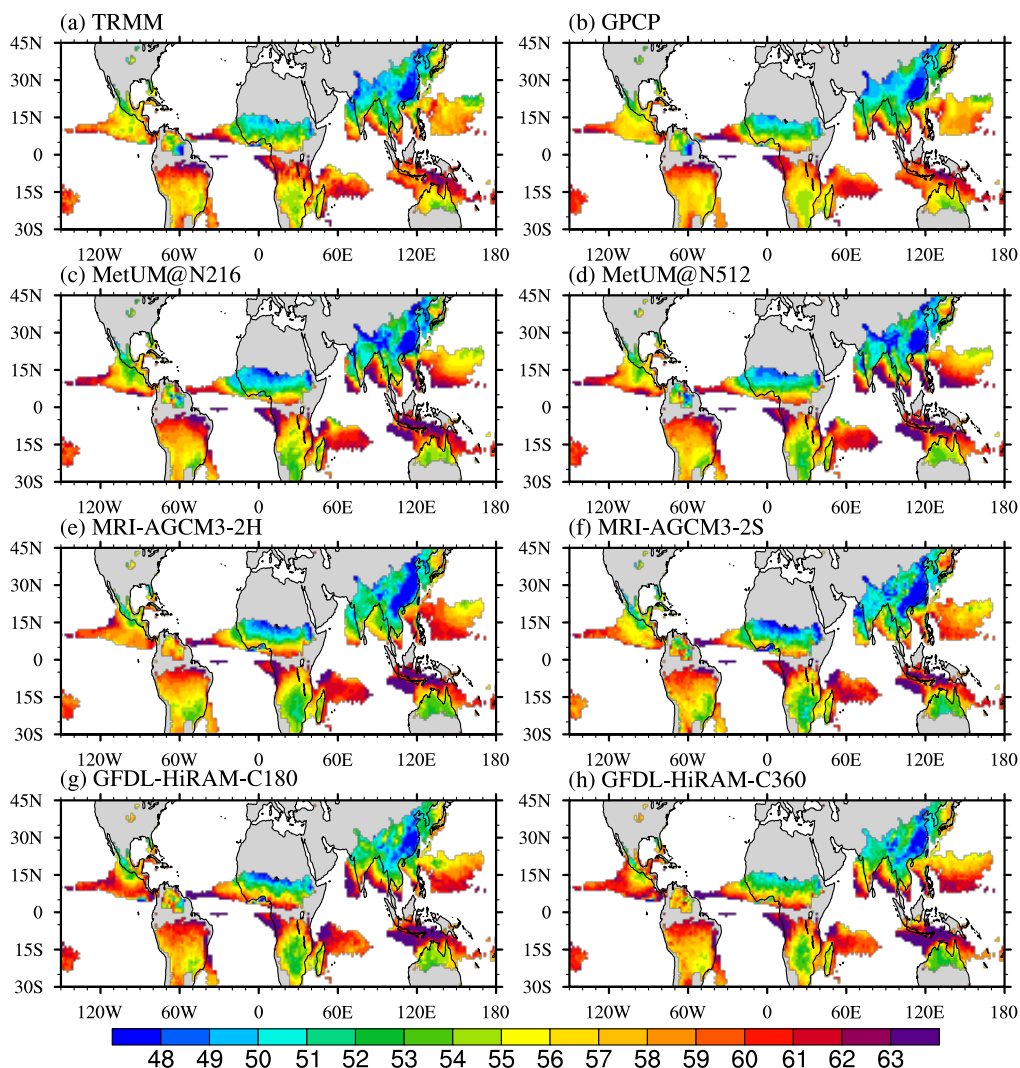


**Figure 9** As in Figure 8, but for the monsoon withdrawal pentad, defined as the pentad with fractional accumulation first becomes  $\geq 0.8$  (Sperber and Annamalai 2014). Note: for Southern Hemisphere locations (Australian, South African, and South American monsoon) the pentads were reordered to July–June prior to the analysis.

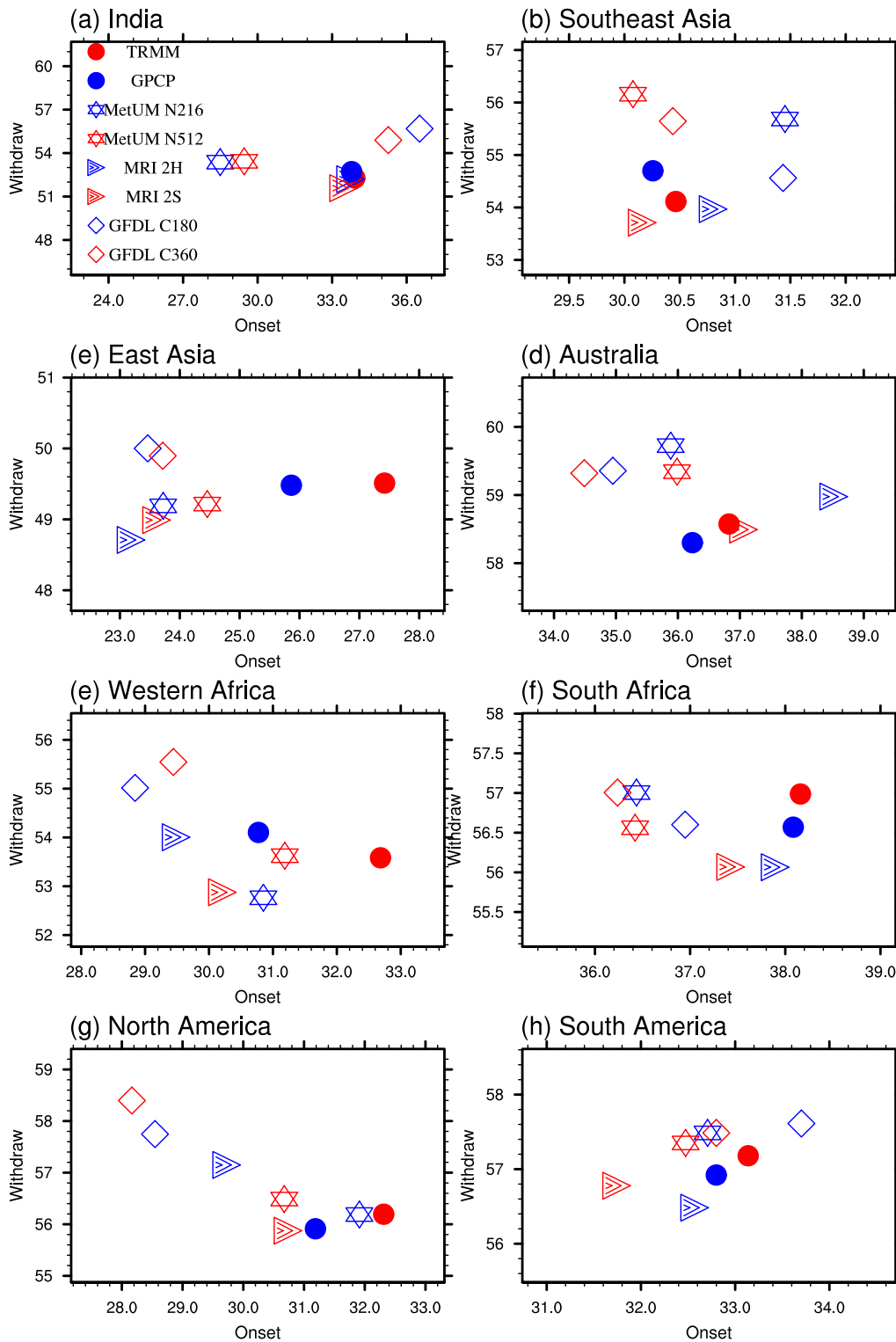


**Figure 10.** The monsoon onset (x axis) and withdraw pentad (y axis) averaged over (a) Indian (India), (b) Southeast Asian (SAs), (c) East Asian (EAs), (d) Australian (Aus), (e) West African (Waf), (f) South African (SAf), (g) North American (NAm) and (h) South American (SAm) monsoon. Note: for Southern Hemisphere locations (Australian, South

1  
2  
3 African, and South American monsoon) the pentads were reordered to July–June prior to  
4 the analysis. The dots, stars, triangles and diamonds represent the results from the observa-  
5 tions, MetUM-GA3, MRI-AGCM3 and GFDL-HiRAM, respectively, with high-resolution  
6 configurations in red and low-resolution configurations in blue.  
7  
8  
9  
10  
11  
12  
13  
14  
15  
16  
17  
18  
19  
20  
21  
22  
23  
24  
25  
26  
27  
28  
29  
30  
31  
32  
33  
34  
35  
36  
37  
38  
39  
40  
41  
42  
43  
44  
45  
46  
47  
48  
49  
50  
51  
52  
53  
54  
55  
56  
57  
58  
59  
60

For Review Only

SAm	0.41,0.20,0.25	0.46,0.19,0.30	0.30,0.02,0.19	0.01,0.01,0.04	-0.1,0.1,1.9	-0.1,0.3,-0.1
NAm	0.32,0.16,0.21	0.31,-0.32,0.69	0.10,-0.25,0.44	0.03,0.03,-0.03	-0.3,-1.3,0.7	0.3,-1.3,0.7
SAf	0.35,0.07,0.26	0.24,0.03,0.27	0.10,0.05,0.01	0.04,0.08,-0.04	0.0,-0.5,-0.7	-0.4,0.0,0.4
Waf	0.16,-0.04,0.14	0.25,0.05,0.19	0.15,0.13,0.18	-0.02,0.04,-0.02	0.3,0.7,0.6	0.9,-1.1,0.5
Aus	0.14,-0.03,0.09	0.57,-0.15,0.46	0.32,-0.07,0.16	0.0,-0.01,0.04	0.1,-1.5,-0.5	-0.4,0.0,0.9
EAs	0.21,0.10,0.13	0.50,0.31,0.47	0.05,0.07,0.14	-0.03,0.02,0.06	0.7,0.4,0.3	0.0,0.3,-0.1
SAs	0.34,0.47,0.30	0.12,0.36,0.68	0.18,0.05,0.17	0.02,-0.03,0.02	-1.4,-0.6,-1.0	0.5,-0.3,1.1
India	0.16,0.64,0.52	0.15,0.85,0.72	0.20,0.07,0.25	-0.02,0.02,0.02	1.0,-0.3,-1.3	0.1,-0.6,-0.8
GM	0.25,0.20,0.16	0.09,0.11,0.11	0.15,0.05,0.17	0.01,0.03,0.01	0.0,-0.6,-0.4	0.2,-0.5,0.1
	ANN	AC1	AC2	Domain	Onset	WithD

**Figure 11** Improvement of the simulation on the annual cycle of global monsoon precipitation with horizontal resolution. Red boxes indicate high-resolution consistently improves performance across all three AGCMs; blue boxes indicate improvements with resolution are inconsistent; orange boxes indicate a better simulation is shown in all three high-resolution AGCMs but the responses to resolution are inconsistent across models. The values from left to right in each box are the difference between high- and low-resolution configurations of MetUM-GA3, MRI-AGCM3 and GFDL-HiRAM, respectively. The metric for the annual modes, including annual mean (ANN), solstitial mode (AC1), the equinoctial asymmetric mode (AC2), is the pattern correlation coefficient with TRMM. The metrics for the monsoon domain and monsoon onset/withdrawal are ETS and the onset/withdrawal pentad, respectively.